FABRICATION AND CHARACTERIZATION OF BARIUM TITANATE

TTHIN FILM ON POLYCRYSTALLINE

NICKEL SUBSTRATE

by

PARISA SAHEBI

Presented to the Faculty of the Graduate School of
The University of Texas at Arlington in Partial Fulfillment
of the Requirements
for the Degree of

MASTER OF SCIENCE

THE UNIVERSITY OF TEXAS AT ARINGTON

August 2013

ACKNOWLEDGEMENTS

I would like to express my deepest appreciation to all those who provided me the help and support in any aspect to complete this research. A special gratitude I give to my supervisor Dr. Efstathios. I. Meletis for his research advises, the useful comments, and remarks and engagement through the learning process of this master thesis. Without his guidance and persistent help this dissertation would have not been possible. I would like to thank Dr. Jiechao Jiang and Mr. David Yan for introducing and guiding me into the field of materials structure characterization and electron microscopy, as well for the support on the way. Also, I would like to acknowledge my committee members, Dr. Fuqiang Liu and Dr. Jiechao Jiang, for their engagement and suggestions.

Furthermore, I would like to thank my group members and friends, Jessica Mooney, Yishu Wang, and Minghui Zhang, for their countless help, encouragement, support, and friendship.

A sincere appreciation I give to MSE staff, Mrs. Jennifer Standlee and Mrs. Lidia Cuauhtli, who have been always more than helpful in many aspects during my masters program.

June 4, 2013

ABSTRACT

FABRICATION AND CHARACTERIZATION OF BARIUM TITANATE

TTHIN FILM ON POLYCRYSTALLINE

NICKEL SUBSTRATE

Parisa Sahebi

The University of Texas at Arlington, 2013

Supervising Professor: Dr. Efstathios I. Meletis

Ferroelectric $BaTiO_3$ (BTO) thin films were deposited on polycrystalline nickel disks and silicon wafer substrates by rf magnetron sputtering. Nickel oxide (NiO) and nanocrystalline nickel (nc-Ni) layers were used as interfacial buffer layers. Microstructural studies with X-ray diffraction and transmission electron microscopy reveal that the BTO films deposited at temperatures lower than 700℃ have an amorphous structure. However, the BTO films sputtered at temperatures higher than 700℃ are partially crystalline. BTO films have a good and continuous interface with both interfacial layers with no interdiffusion or reaction with the substrates. In the case of BTO deposition with nc-Ni interlayer at higher deposition temperature of 800℃, a thin NiO layer forms between the nc-Ni and BTO films. Having nc-Ni as an interfacial layer enhances surface morphology and decreases surface roughness. This study shows that nc-Ni can act as a proper interfacial layer between a ceramic like BTO and the metallic substrates and is a better alternative for NiO buffer layer.

TABLE OF CONTENTS

LIST OF ILLUSTRATIONS

LIST OF TABLES

Chapter 1

INTRODUCTION

Ferroelectric (FE) materials are of interest for a number of applications, including non-volatile memories, dynamic random access memories (RAMs), electro-optic switches, pyroelectric detectors, optical modulators, shutters, optical mixers, sensors, imagers, and displays to name a few. Recently high quality ferroelectric thin films (FETF) have been used for the development of advanced microwave signal processing devices [1]. Since in a FE material, the dielectric constant (ε') can be varied by applying a d.c. electric field, it allows device characteristics to be 'tuned' in real time for particular application, e.g. resonators and delay lines. Thin films offer a unique advantage over bulk materials for these applications. Small, compact, low power microwave devices that can be fabricated from structures based on FE films include phase shifters, tunable filters, tunable resonators, phased array antennas, and frequency agile microwave radio transceivers [2]. Barium titanate, BTO, in thin film form promises to meet most, if not all, of these needs because of its special nature and unique combination of properties.

Barium titanate is one of the most important ferroelectric materials and has attracted much attention for its remarkable properties, such as high dielectric constant, good ferroelectric properties, and large electro-optic and nonlinear optic coefficients [2-4]. These unique properties make BTO thin films to be a great candidate for development of advanced microwave signal processing devices, as well as the unobtrusive piezoelectric water active sensor array for structural health monitoring [1-6]. However, major challenges exist since the fabrication of the ferroelectric BTO thin films on structural materials raise a number of crystallinity and interface-related issues [6-7]. In order to resolve this problem, an ultrathin interfacial buffer layer of NiO has been used to facilitate the BTO film growth by bonding it onto Ni substrate. NiO has a rocksalt structure with an excellent electrical conductivity and chemical stability, which can be

1

used as conductive electrode and as a barrier for blocking the interdiffusion or inter-reaction between the ferroelectric film and metal substrate. A new approach to this issue, which was explored in this research, is to use nanocrystalline nickel as the interfacial buffer layer. Since nanocrystalline materials have high density of grain boundary, they provide high potential energy locations for nucleation and growth of BTO crystals. This theory was studied as the major purpose of this research.

Chapter 2

LITERATURE REVIEW

2.1 Ferroelectric Properties of Barium Titanate

Barium Titanate ($BaTiO_3$) in tetragonal form is a displacement type FE material, for which the origin of ferroelectricity is derived from the displacement of ions relative to each other. The most remarkable property of $BaTiO_3$ is its high permittivity. The room temperature dielectric constant of $BaTiO_3$ ceramics is known to be greater than 2000 [3]. However, there are three major differences between thin films and bulk materials. First, the thin film dielectric constant is lower than bulk FE materials by a factor of five or more. Second, the temperature dependency of the dielectric constant is much broader in thin films. Finally, the Curie temperature, T_c, of thin film FE is shifted. Most of the reported works, however, have failed to obtain $BaTiO_3$ thin films with high permittivity in comparison to bulk $BaTiO_3$ ceramics. Recent success in depositing high quality $BaTiO_3$ thin films on insulating substrates has brought the photonic application of $BaTiO_3$ to reality [4]. However, for electronic applications, the deposition of $BaTiO_3$ thin films on conducting substrates has been used.

$BaTiO_3$ thin films have been prepared by methods such as hydrothermal, pulsed laser deposition, metalorganic chemical vapour deposition (MOCVD), r.f. magnetron sputtering, argon ion beam sputtering, molecular beam epitaxy, excimer laser ablation, partially ionized beam technique, evaporation, electrochemical, and sol-gel. Among these methods, sol-gel processing and RF magnetron sputtering have the edge over other deposition techniques. Sol-gel processing is known for producing good homogeneity, ease of chemical composition control, high purity, low temperature processing, and large area. RF magnetron sputtering's capacity of depositing thin films over a large substrate area, as well as its low cost, simplicity and reproducibility has made this method very

significant and applicable [5].

While there are problems with $BaTiO_3$, films such as leakage current, the electrical conduction mechanism in them is not yet very well understood despite extensive studies. The electrical properties of the films have been found to depend on the preparation technique, processing conditions and substrates used. The typical problem in understanding $BaTiO_3$ thin films is the large variation (100 to 2500) in the reported values of the room temperature dielectric constant (Table 2.1). The anomaly in this large variation of room temperature dielectric constant, however, could not be clearly identified. The possible reasons may be due to the complex relation between processing techniques, substrates, deposition conditions, etc., and the grain size of the films and its growth characteristics [6].

Table 2.1 Dielectric constant of $BaTiO_3$ thin films produced using various fabrication techniques [6]

Deposition technique	Substrate	Annealing temperature (°C)	Thickness (μm)	Dielectric constant	Reference
Evaporation	Pt	1000	1–2	225	[22]
Hydrothermal	Ti/Si	100–200	0.2–1	450–550	[25]
Pulsed laser	Pt/Si	750	0.493	485	[26]
MOCVD	Pt/MgO	As depo	0.3–0.8	100	[13]
	Si	450	0.2	1157	[27]
R.F. magnetron sputtering	Pt		0.21–2	750–2500	[28]
	RuO$_x$/Si	680	0.273	290	[29]
	Pd/Si	700	2	330	[30]
	Si	650	1	120	[31]
Sol-gel	stainless steel	600	0.5	150	[32]
	Pt/SiO$_x$/Si	650	0.5	800–1000	[33]
	BaPbO$_3$	800	0.4	600	[34]
	Ti	850	0.3	210	[35]
	Ti	400	0.3	90	[35]
	Pt	750	2.5	521	[24]
	stainless steel	700	0.7	300	[24]

Thomas et al. [6] prepared barium titanate sol using chemical solution deposition (CSD) and spin coated the sol on p-type single crystal silicon (100) wafers, stainless steel, and fused silica substrates to obtain polycrystalline, transparent, and crack-free films. They examined the crystallinity of the films by X-ray diffraction (XRD). The pyrolysed films (~400°C) were amorphous, and post deposition annealing was required to develop crystallinity. Annealing temperature effects were studied using a series of films deposited on fused silica. Figure 2.1(a) shows the XRD patterns of the $BaTiO_3$ films on fused silica annealed at various temperatures.
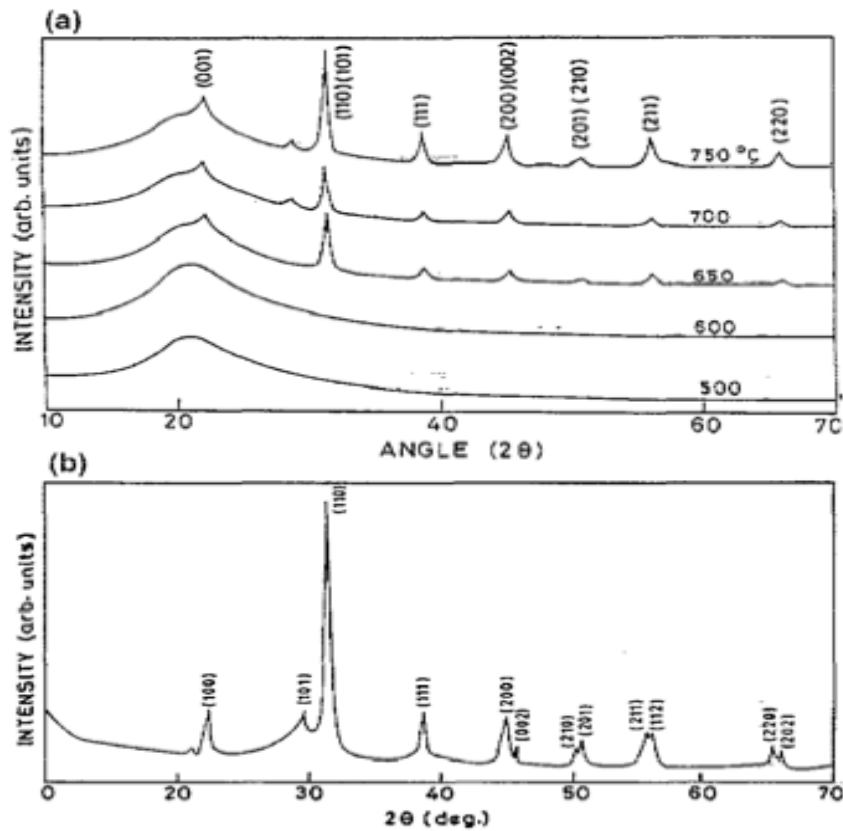
Figure 2.1 (a) X-ray diffraction patterns of $BaTiO_3$ films on fused silica annealed at various temperatures. (b) X-ray diffraction pattern of $BaTiO_3$ films on fusel silica annealed at 700°C [6].

From the patterns of XRD, the polycrystalline nature of $BaTiO_3$ can be confirmed when annealed between 650 and 750°C. A better understanding has been achieved regarding the annealing temperature and crystallization through the optical properties.

The optical band gap was found to be 3.75 eV for 650°C annealed film. Optical characterization shows that scattering losses contribute to the total optical losses when grain growth occurs at elevated temperatures. The observation of a butterfly loop in the C- V curve and P-E hysteresis (Figure 2.2 and 2.3) suggests the ferroelectricity and tetragonal structure of BaTiO3 film.
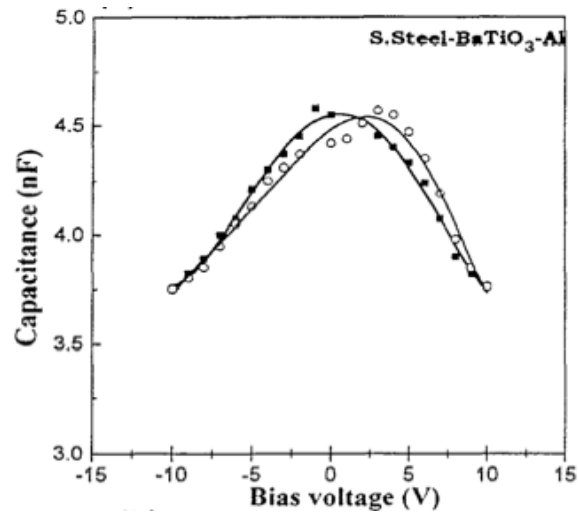
Figure 2.2 The effect of applied bias field on the capacitance of a sol-gel derived $BaTiO_3$ film on stainless steel substrate [6].
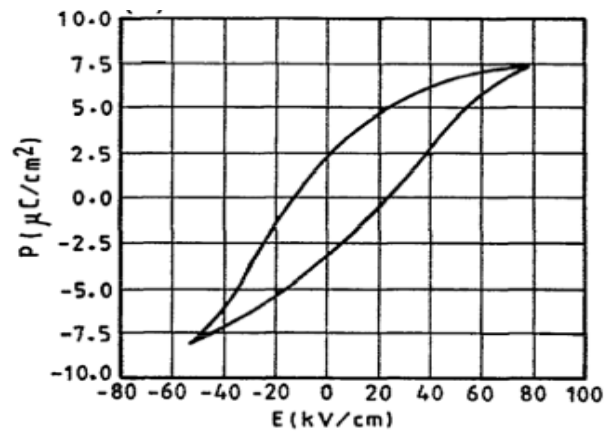
Figure 2.3 P-E hysteresis of $1\mu m$ thick $BaTiO_3$ film on stainless steel [6].

Dielectric constant values of 66 and 140 were obtained at 1MHz for films on p-silicon and stainless steel, respectively. The optical constants (refractive index, n and absorption coefficient, k) vary with the annealing temperature. This variation is in the 300–750°C thermal range. They also showed that n grows from 1.75 to 2.5 ($\lambda = 610$ nm) in this annealing temperature range. The refractive index of the thin film is proportional with its electronic polarization, which is inversely proportional with the interatomic spacing. In this sense, a reduction in the interatomic spacing that results in the densification of the film (with reduction of porosity) leads to an increase in the refractive index. They pointed out a sharp increase in the 600– 700°C range due to the crystallization of the perovskite phase. Debye type relaxation process was observed for films on stainless steel substrates with activation energy of about 0.34 eV. The conduction mechanism of $BaTiO_3$ films in MIS and MIM configurations was studied and was found due to space charge limited current. The current followed Ohm's law in the low voltage region. At high voltages, the MIS structure showed a square law dependence of current on voltage, which is attributed to the SCL current controlled dominantly by the empty traps near the conduction band. However, for the MIM structure the $V^{5/2}$ dependence of the current suggests the involvement of deep trap levels in the conduction process, which is the result of a set of traps distributed exponentially from the bottom of the conduction band edge.

Ianculescu et al. [7] deposited $BaTiO_3$ thin films on Pt/Ti/SiO_2/Si by rf magnetron sputtering. Post deposition annealing of the samples was carried out in air, at 900°C for 8 h in order to obtain crystalline films. The annealed films present band gap energy in the range of 3.57–3.59 eV. In the 2D image of the sample (Figure 2.4), it can be noticed that the one-layer deposition followed by annealing, leads to a great number of small dark spots, which represent depression zones with an average size of 230 nm, having a circular geometry and uniformly distributed on the film surface, which seems to be relatively smooth. Indeed, the root mean square roughness (RMS) value is only of 10.6 nm.
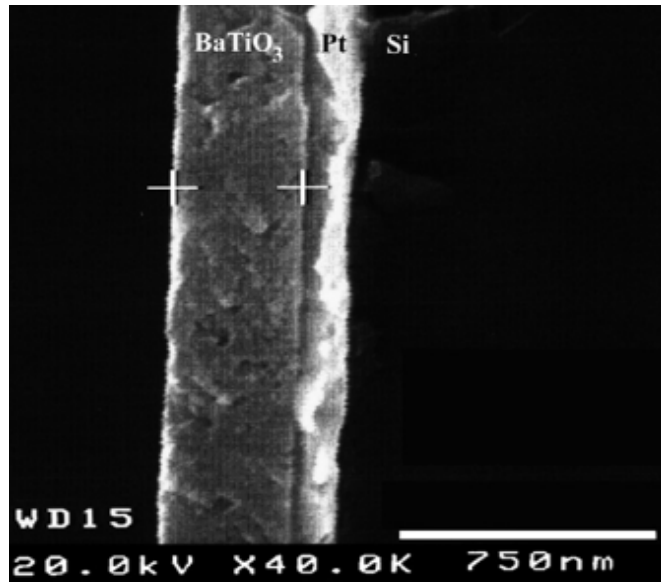
Figure 2.4 Cross-section SEM micrograph [7].

The roughness values (10–20 nm) of the surface layer estimated from spectroscopic ellipsometry (SE) and atomic force microscopy (AFM) measurements were in good agreement. The obtained films have tetragonal unit cell and show densely packed, non-columnar morphology and hexagon-like crystallite shape.
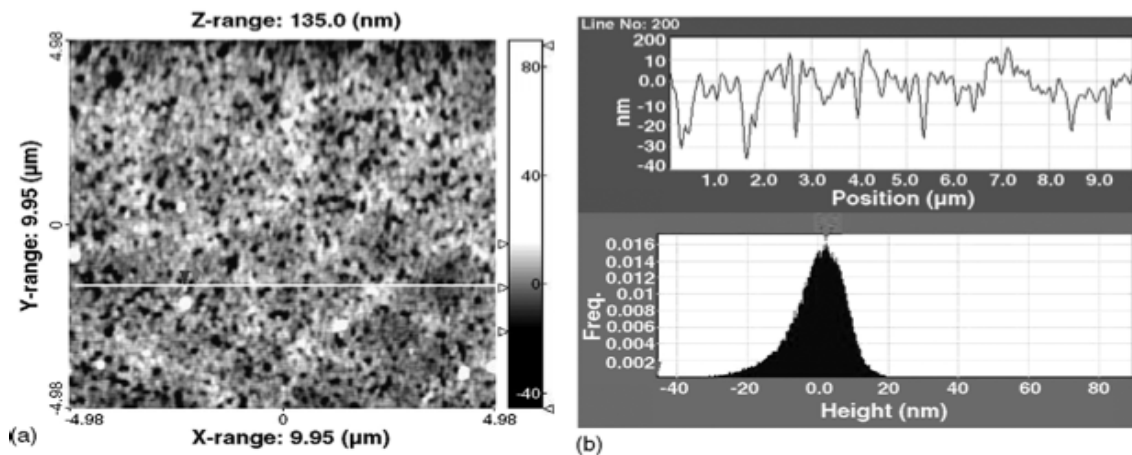
Figure 2.5 AFM micrograph of BaTiO_3 thin film: (a) 2D view and (b) profile across the surface and height distribution histogram [7].

The Ba/Ti ratio has important influence on the phase composition of films crystallized by annealing [8]. BaTi$_2$O$_5$ secondary crystalline phase can be obtained by

8

annealing of nonstoichiometric films at high temperatures. Formation of $BaTi_2O_5$ phase implies important microstructural changes with some possible consequences on the electrical behavior of the films. $BaTi_2O_5$ favors a decrease of the film porosity by filling in the voids between the columnar $BaTiO_3$ crystals. In turn, this could lead to improvement in some electrical properties (such as decrease in the leakage current values) of these films although other properties might be affected (dielectric constant).

Berg et al. [9] deposited $BaTiO_3$ thin films on Si/SiO2/Ti/Pt/Au/Pt templates at different temperatures in the range 560–680 °C by pulsed laser deposition. Cross section scanning electron microscopy images and AFM surface morphology analysis reveal films with columnar structure and in-plane grain size distribution, in the range 10–60 nm, depending on growth temperature. They performed low-field dielectric measurements as functions of temperature in the range 40–500°C and external dc field up to 400 kV/cm. The apparent permittivity of ferroelectric films grown at 680 °C shows Curie–Weiss behavior above 400°C with Curie temperature of 240°C. The films grown at lower temperatures reveal a decrease of Curie temperature down to −80°C, reduced values of apparent permittivity and loss tangent, and broadening of maximum of temperature dependence of apparent permittivity. The film grown at 590 °C demonstrates state of the art combination of temperature stability (temperature coefficient of apparent permittivity 300 ppm/K in the range 50-350°C), high tunability of apparent permittivity (up to 60% at room temperature), and relatively low loss tangent (less than 0.05 in the frequency range up to 10 GHz). Figure 2.6 shows the apparent permittivity, ε_a, as a function of applied external field, E_{ext}, for films grown at different temperatures, ranging from 560 °C to 680 °C. The apparent permittivity is calculated as $\varepsilon_a=Cd/\varepsilon_0A$, where A is the area of the inner top electrode. Some hysteresis effects are visible, indicating contribution of irreversible polarization. The main observation is that the permittivity maximum is changing dramatically with the growth temperature, as is clearly seen in Figure 2.7 where the maximum permittivity is plotted as a function of the growth temperature. The permittivity increases almost linearly from about 20 for the film grown at the lowest temperature to about 900 for the film grown at the highest temperature.
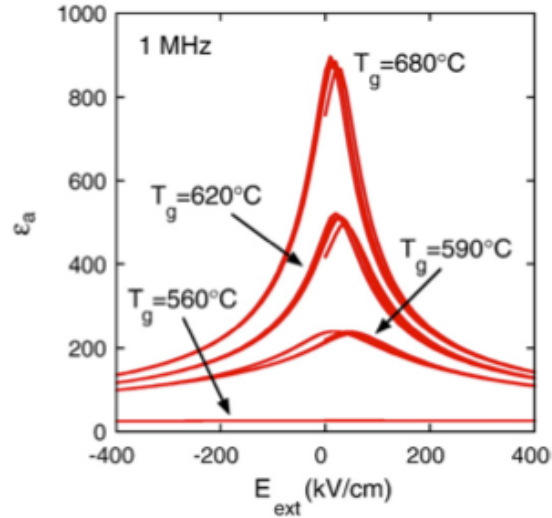
Figure 2.6 Apparent permittivity as a function of applied external field, measured at room temperature and 1 MHz frequency for BTO films grown at different temperatures, as indicated in the figure [9].
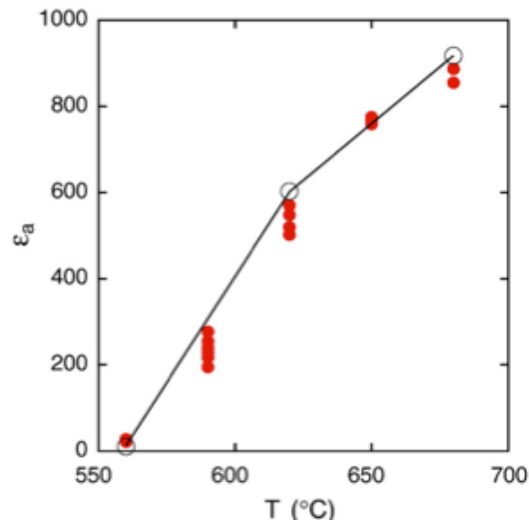
Figure 2.7 Apparent permittivity as a function of BTO film growth temperature. Filled circles: Dielectric measurements performed at room temperature and 1 MHz frequency. Open circles: Columnar composite model [9].

Figure 2.8 shows a typical cross section SEM image revealing a BTO film with a pronounced columnar structure, with columnar grains growing from the bottom electrode to the surface of the film. The columnar structure is observed for all films, even for the

film grown at the lowest temperature, which judging from the very low permittivity, mainly is amorphous. (Predominantly amorphous state of BTO film grown at lowest temperature is confirmed by preliminary results from cross section TEM studies.) The thickness of the films was found to be close to 500 nm.
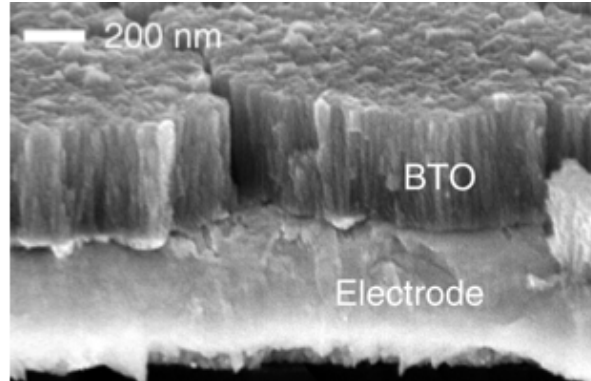
Figure 2.8 Typical cross section SEM image of BTO film [9].

To obtain a suitable nonlinear optical material which has high susceptibility, a possible strategy is to incorporate the larger volume fraction of metallic particles into the matrix and control the shapes and sizes of metallic particles. Sol-gel technique is a suitable method for preparation of nanocomposite materials embedded with metallic particles. With this method, it is possible to increase the volume ratio of metal particles in matrix films and control the size and shapes of the particles [10]. Figure 2.9 shows the XRD patterns of $Au/BaTiO_3$ thin films coated on glasses heat-treated at different temperatures ranging from 200 to 600°C. Two peaks at 2h = 38.3° and 44.5°, which corresponds to Au(111) and Au(200) crystalline planes, respectively, can be identified in the films annealed at 400 and 600°C, but are not clear in the films annealed at 200°C. This implies that Au nanoparticles could crystallize out at above 200°C. The characteristic diffraction peaks of $BaTiO_3$ matrix cannot be found in the scanning range, which indicates that $BaTiO_3$ matrix remains amorphous up to 600°C. Average size of Au nanoparticles is 20 nm. Figure 2.10 shows the absorption spectra of films with different

heat-treatment temperature, which indicates different absorption peaks at 569.5 nm (200°C), 579.5 nm (300°C), 583.5 nm (400°C), 595.5 nm (500°C), 605.5 nm (600°C). The absorption peaks shift to longer wavelength in accordance with the increase of heat-treatment temperature, which is believed to be related to the surface plasma resonance of Au metal particles. The nonlinear optical properties of these films ware measured and the values of susceptibility were calculated to be in the range of $10^{-8} - 10^{-9}$ esu.
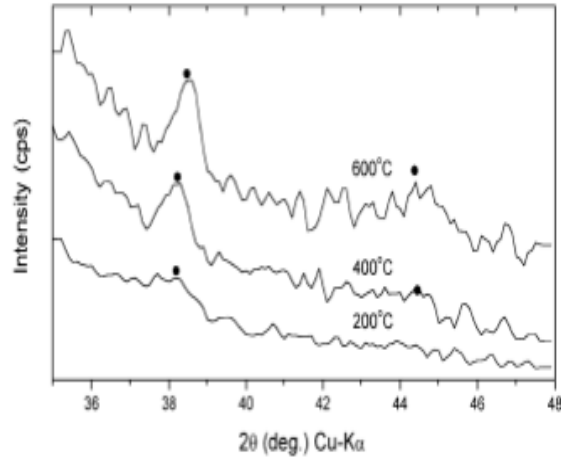
Figure 2.9 XRD patterns of Au/BaTiO3 films coated on glasses with different annealing temperatures [10].
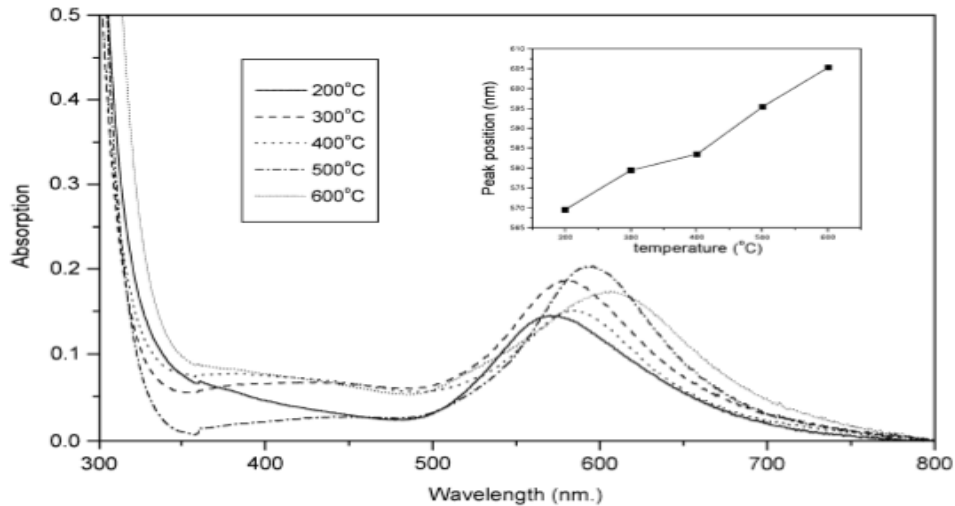
Figure 2.10 Absorption spectra for different heat-treatment temperatures of Au/BTO films [10].

Low leakage ferroelectric BaTiO$_3$ thin film capacitors can be fabricated by deposition of multilayer BTO thin films with different microstructures and thicknesses ranging from 220 nm to 265 nm using reactive r.f. magnetron sputtering [11]. Layers of BTO deposited at low temperature are amorphous and those deposited at high temperature above 600°C are polycrystalline. Microcrystallization of amorphous BTO took place at a thermal treatment temperature of above 600°C. Capacitors with a configuration of Au/BTO/RuO_2/SiO_2/Si, as shown in Figure 2.11 were used to determine the dielectric and electric properties of BTO thin films.

Nanolayer A/$(P/M)_n$, n=1,2,3,… and bilayer P/M ferroelectric BTO thin film capacitors take advantage of the best properties from both amorphous and polycrystalline materials through processing and device design. Hysteresis measurement confirmed the ferroelectric properties of BTO films. It can be extracted from Figure 2.12 that the dielectric constant is in the range of 39-60, which is a function of the device configuration and the ratio of sub-layer thickness. Figure 2.13 shows how dielectric loss of capacitors is dependent on the configuration. The d.c. conductivity of films with a thickness in range of 220-265 nm is less than $10^{-13}\Omega^{-1}cm^{-1}$ at a field strength of $2\times10^5\ Vcm^{-1}$. The breakdown voltage is above $10^6\ Vcm^{-1}$. The leakage current density of the films is in the range of 10^{-10} to 10^{-8} Acm^{-2} at a field strength of $2\times10^5\ Vcm^{-1}$. All of these data show the promise of BTO as a dielectric in very large scale integrated circuits.
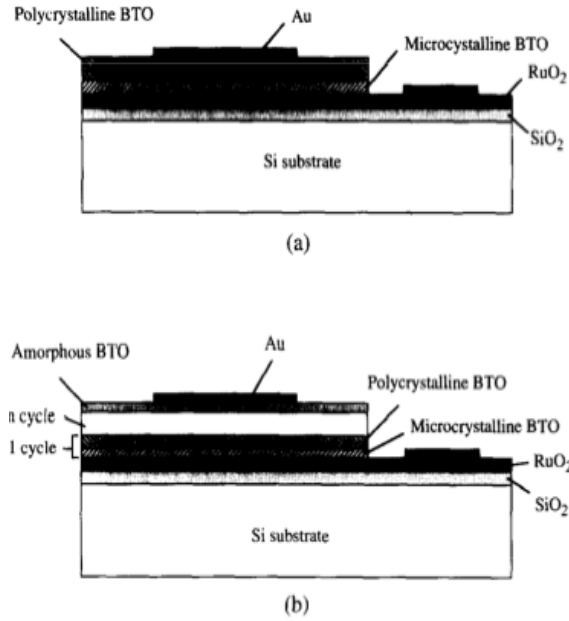
Figure 2.11 Different capacitor constructions designed to reduce the leakage current and maintain the high dielectric constant of the dielectrics: (a) a bilayer of polycrystalline on microcrystalline structure (P/M); and (b) a nanolayer with amorphous structure on a number of stacked cycles of polycrystalline on microcrystalline layers (A/$(P/M)_n$, n=1,2,3,…) [11].
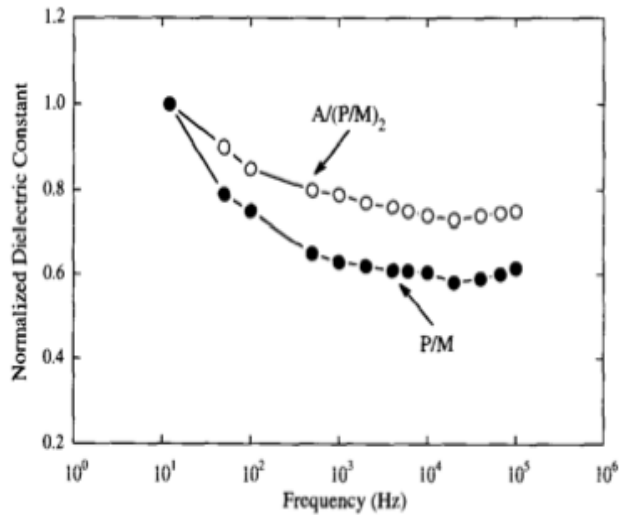
Figure 2.12 Frequency-dependent dielectric constant for the capacitors with different configuration of P/M and A/$(P/M)_2$ [11].
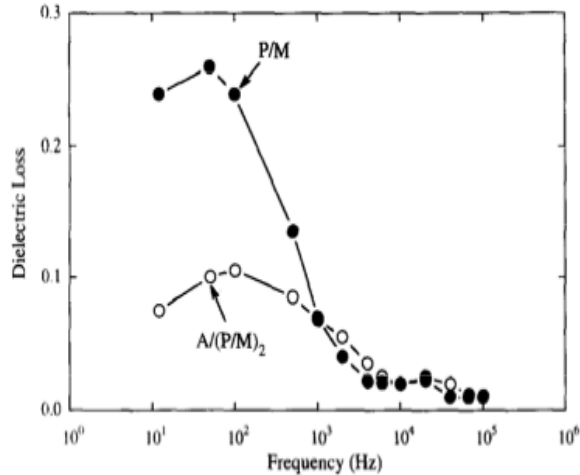
Figure 2.13 Frequency-dependent dielectric loss for the capacitors with different configuration of P/M and $A/(P/M)_2$ [11].

2.2 Physical Vapor Deposition of Barium Titanate

PVD is a variety of vacuum deposition methods used to deposit thin films by the condensation of a vaporized form of the desired film material onto various specimen surfaces (e.g., onto semiconductor wafers). The coating method involves purely physical processes such as high temperature vacuum evaporation of target material with subsequent condensation, or plasma sputter bombardment rather than involving a chemical reaction at the surface to be coated.

Variants of PVD include:

▪ Cathodic Arc Deposition: in which a high power electric arc is used to vaporize material from a cathode target. The vaporized material then condenses on a substrate, forming a thin film of metals, ceramics, and composites.

▪ Electron Beam Vapor Deposition: in which a target anode is bombarded with an electron beam given off by a charged tungsten filament under high vacuum. The electron beam causes atoms from the target to transform into the gaseous phase. These atoms are transported by diffusion to be deposited by condensation on the specimen.

15

▪ Evaporative Deposition: in which the material to be deposited is heated to a high vapor pressure by electrical resistive heating in low vacuum.

▪ Pulsed Laser Deposition: a high power pulsed laser beam is focused inside a vacuum chamber to strike a target of the material that is to be deposited. This material is vaporized from the target (in a plasma plume), and deposited as a thin film on a substrate.

▪ Sputtering Deposition: In which a glow plasma discharge (usually localized around the target by a magnet) bombards the material sputtering some away as a vapor for subsequent deposition.

Thin film technology is a large branch of the generic technology that has to do with surface modification and coating. In the surface modification process the properties of the surface of the substrate material is changed and to know these properties, one should consider the role of some parameters, such as background pressure, concentration of impurities in the vapor phase, kinetic energy of the incident particles, deposition rate, nature of substrate material, temperature of the substrate and its surface cleanliness, orientation and microstructure. The final properties of the material are sensitively dependent on the defect structure of the film, which in turn depends on the process used to obtain the film.

PVD methods for thin film deposition fall into four stages:

▪ First Stage- Principles and methods underlying the formation of the vapor phase from the condensed phase and the properties of the vapor; evaporation, electron beam evaporation, sputtering, ion deposition and so on typify some methods of vapor creation.

▪ Second Stage- Transport of atoms or molecules from the source of the substrate; techniques, such as reactive evaporation, activated reactive evaporation, electron cyclotron resonance plasma assisted growth and others focus on alternating the evaporated atoms before they reach the substrate.

▪ Third Stage- Deposition of atoms on the substrate; the major area of thin film technology is concerned with the ability to grow an epitaxial film on

a substrate. This ability gives us an unique control on the composition and structure and defects of the thin film, as well as geometrical manner in which film can be deposited so that fabrication of devices become easy and economical.

▪ Fourth Stage- Processes for rearranging the atoms on the film or reconfiguring the geometry of the film to give the desired properties for the product; the control of microstructure of thin films, the ability to place defects as desired or eliminate them all together, to control surface morphology, to induce the needed crystallographic alignment, and to etch a film as desired represent a short list of attributes that are desired in the final microstructure of the film. Annealing on the film to control grain growth, altering the stoichiometry of the film, introducing dopants and oxidizing the film, and inducing compressive stress in the film are some of the reasons for post-film deposition processing [12-14].

i. Evaporation

Evaporation of a material and its subsequent condensation on a substrate is one of the simplest processes for thin film deposition. In this method, the material to be deposited is in the form of a solid or liquid phase and requires thermal energy for transformation into the vapor phase. Evaporation thus incudes sublimation when a solid directly transforms into vapor and vaporization when the liquid transforms into vapor on thermal treatment. The vapor, by its own nature, expands into an evacuated chamber that contains the substrate and condenses on the substrate that is at lower temperature than the evaporation source.

Even when the energy that is supplied to the evaporant may come from electrons or photons, the vaporizing mechanism may still be thermal in nature. Thin film deposition sources, such as electrical energy or electron beams, are the means to bring about a phase change of a material from the condensed phase to the vapor phase. Recently, in most of Physical Evaporation Deposition systems, target material is heated directly by a laser beam. The success of this technique in depositing multicomponent superconducting material thin films has prompted the investigation of deposition of a

wide variety of materials, consisting of many components [12,13].

ii.   Cas-Solid Interactions

The material can interact with the gases and change the environment. Conversely, the environment can influence the material and change its properties. A clear understanding of a number of phenomena is necessary to appreciate the conditions under which solids take up gases and release gases. These phenomena are: evaporation and condensation, adsorption and desorption, back scattering, displacement, surface reactions, solubility, diffusion, permeation, degassing and leaks. These phenomena are showing schematically in Figure 2.14. A gas in the environment can interact with a solid in a number of ways. One of the ways is by the formation of a gaseous product, e.g. hydroxides decomposition in high temperature, resulting in the removal of gases from the solid. Alternatively, a solid can remove a gaseous product from the environment, e.g. gas chemisorbing of finely divided alumina from the environment. Some gases interact with the solid and in return react and form a new gaseous product. In certain situations, reactions between gases in the environment can occur by catalytic effect of the solid present, without the consumption of solid in the process. Gas adsorbed on the surface of a solid can also desorb from this surface. Desorption is the release of the gas from internal surfaces to the vacuum chamber, when the molecules are held in bound stated on surfaces of a solid. The mechanical properties of the material can drastically change because of the dissolution of the gas in the solid. Volume changes invariably accompany phase changed that result in uneven stresses in the material promoting unexpected dimensional changes or crack propagation. It would be desirable to start the deposition of a film in a chamber where there is very little gas to begin with, as in a high vacuum, so that contamination problems can be avoided. It is clear that the materials that can easily evaporate within the chamber and contribute to the gas load in the system should be avoided in the vacuum system. The gases can dissolve in the solids and their concentration is a function of pressure, temperature, and the nature of the gas and the solid [12,13].
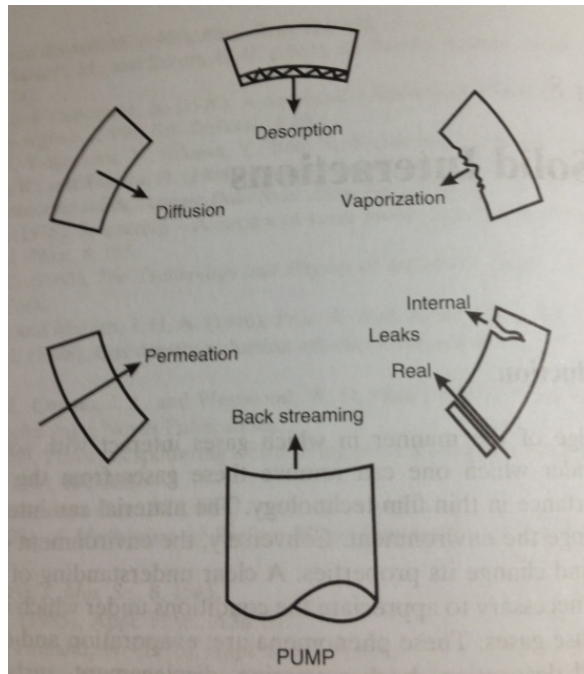
Figure 2.14 Potential sources of gases and vapors in a vacuum system [12].

Every surface has, at any finite temperature, atoms vibrating about their equilibrium positions. Near the surface, some atom may possess sufficient kinetics energy momentum in the direction normal to this surface to escape from the surface. There will be a dynamic balance between the atoms wanting to recondense onto the solid with the atoms wanting to leave the surface of the solid.

A gas molecule striking a solid surface can either be reflected by an elastic collision or may temporarily stay on the surface and subsequently depart with a velocity and direction that is unrelated to its initial values. The energy transfer between the gas molecule and the atoms I the solid occurs only in the latter case. Sorption is the name given to the type of interaction by which the gaseous molecule resides in/on a solid. Adsorption refers to the type of interactions that the gas molecule has with the atoms of the solid surface whereby the molecules will spend a larger proportion of their time near the surface than in the bulk of the gas phase. When the gas atoms penetrate further into the solid and there is a volume dependency, then one speaks of occlusion or adsorption. Two classifications of adsorption are generally popular: physical adsorption and chemisorption. In physical adsorption, the exchange of energy that occurs when a gas

atom settles on a vacant position on the solid surface is analogous to the energy of condensation of gas atoms. In chemisorption, the gas atom may combine with the surface atom on a solid to form a chemical compound so that the energy involved corresponds to the heat of formation of a compound. In a real situation, the picture of adsorption of gases shows a continuous variation from physical adsorption to chemisorption. Physical adsorption generally does not result from any major rearrangement of the electron clouds of the gaseous atoms or molecules. Furthermore, no splitting of the molecules into the parts occurs. The amount of the heat released in physical adsorption corresponds to heats of condensation of gas and is generally within 1-20 kJ/mol. Physical adsorption can occur only below the critical temperature of the gas. The nature of forces responsible for this adsorption is van der Waals type of forces. The attractive forces is therefore provided by the instantaneous dipole moments of the adatom and its nearest neighbor surface atoms. Physical adsorption is generally rapid and reversible by lowering the pressure. One important feature of physical adsorption is that multilayer formation occurs here [12,15].

iii.   Nucleation and Growth of Films

Whenever a molecule is incident on the surface of a condensed phase, there are a number of outcomes, which do not involve the molecule to stay on the surface of any extended period. Every square meter of surface exposed to atmospheric pressure will be collided with molecules at the rate if 10^{28} per second. These interactions are classified generally under the category of classical scattering, inelastic scattering and trapping (Figure 2.15) [12]. Whenever the period for which the molecules stay on the surface is extended, we have to differentiate several types of phenomena, such as thermal accommodation, sticking, adsorption, surface diffusion, surface chemical reaction, and nucleation and kinetics of growth [16].

One of the major considerations in thin film deposition is an understanding of the factors that contribute to the development of grain structure and its properties in thin films. The details of the development of grain structure and its properties in thin films are of crucial importance for the application of films. The formation of thin film is

accomplished in three stages. The first stage is nucleation during which small nuclei are formed and are statistically distribute over the substrate surface. The nuclei thereafter grow in size and form large islands of deposit. Eventually the islands coalesce and form a more or less continuous film. In the general case, we have to treat the condensation from a supersaturated vapor onto a solid, which is usually of a different material than the vapor. The phenomenon is referred to as heterogeneous nucleation. The first step in transforming a supersaturated parent phase to a stable daughter phase is the formation by fluctuation of aggregates of the daughter phase on the substrate. The fluctuations are generally classified as homophase fluctuations or heterophase fluctuations. In the homophase fluctuations, the aggregates of small molecules appear to be no different than the parent phase of the system. In heterophase fluctuations, fluctuations occur that are recognizable as belonging to another phase. When the vapor phase is stable, the density of heterophase fluctuations is small and they have a tendency to decay. As the conditions of temperature and pressure that favor the condensation of a vapor to a solid are reached, the heterophase fluctuations grow in density. These fluctuations are called clusters [17].
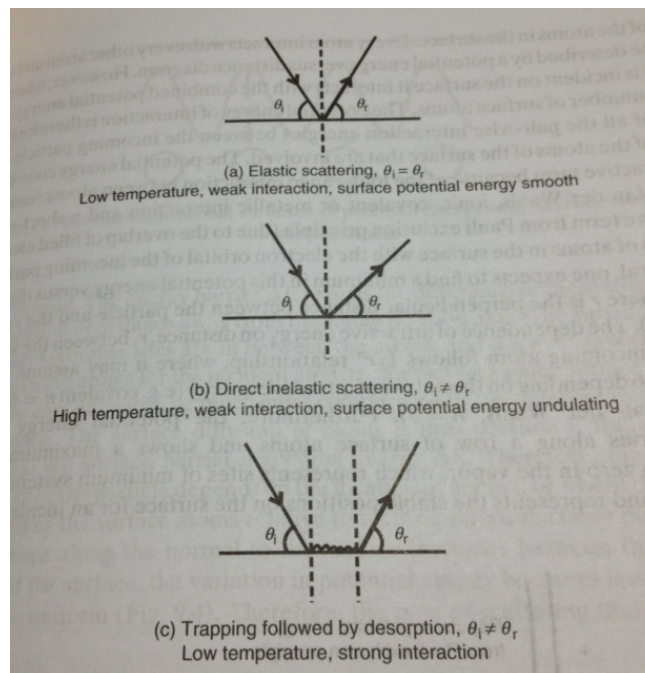
Figure 2.15 Types of interaction of gas molecules with a surface: (a) Elastic scattering, (b) Inelastic scattering, (c) Trapping or desorption [12].

The incident atom transfers its kinetic energy to the substrate and become adatom. The loosely bound adatom has to traverse on the substrate surface by surface diffusion. In this process the adatom exchange energy with the atoms on the substrate, or join with other adsorbed atoms or get trapped in some low-energy sites on the substrate. The atoms that are incorporated can also readjust their location by a bulk diffusion process. Polycrystalline films are described in terms of its grain size, grain boundary, morphology, and film texture. Polycrystalline films form when the substrate is amorphous or covered with an adsorbed contaminant layer and whenever the epitaxial film is not likely. The deposition rate and the substrate temperature are tow important parameters that in a large measure determine the microstructure of the film. The ratio of the time interval to deposit a single layer of film to the time it takes for adatom to encounter other adatoms that are diffusing is important in determining the microstructure. The surface diffusion of atoms, the bulk diffusion and desorption are characterized by activation energy for self-diffusion, activation energy for bulk diffusion, and activation energy for sublimation, respectively. Each of these energies has a very good correlation to the melting point, T_m, of the material. The importance of one process or the other to be dominant depends on temperature T of the substrate. Microstructures of films are thus expected to show a common dependency on T/T_m. These considerations determine the degree to which adatoms are able to seek out minimum energy positions and grain boundaries are able to adjust to their minimum energy configurations. Grain size, grain orientation, grain shapes and their distributions play an important part in determining the properties, performance and reliability of a polycrystalline film. Magnetic properties, mechanical properties, and resistance to electromigration are some of the important commercial interests that require careful study of grains in films and their formation. The nature of substrate (epitaxial or nonepitaxial), the impurity levels of the film, the temperature of the substrate, the presence or absence of ion bombardment, and the use of magnetic or electric fields are among the process variables that are utilized to control the behavior of grains [12,16].

2.3 Magnetron Sputtering of $(Ba,Sr)TiO_3$ Thin Films

Magnetron Sputtering is a physical vapor deposition (PVD) process, where atoms from a target are ejected by high-energy ion bombardments and deposited onto a substrate (Figure 2.16). After the vacuum chamber is evacuated, a sputtering gas -- typically argon-- is introduced into the chamber. Several kilovolts of dc bias is applied to the negative terminal of the magnetron gun, which accelerates the electrons towards the anode. The electrons follow a cycloidal path on the cathode with the applied magnetic field and collide with argon atoms. The electrons with high enough energy can knockout electrons from argon molecules and convert them into positively charged ions (Ar+). The positive Ar+ ions are driven to the cathode where they collide with the target atoms and sputter them through momentum transfer. The plasma is initiated by the multiplication of these collisions. The chamber pressure is usually kept at between 5-50 millitorrs during sputtering. After a visible plasma is obtained, a current flows and the target material is deposited onto the surfaces with higher potential energy than that of the cathode (i.e. substrate). The dc discharge is sustained due to the generation of ion-induced secondary electrons at the cathode. If an insulating material is used as the target material, a practically impossible amount of dc voltage (~1012 V) is needed to achieve the same current density as in a conducting target [18]. This barrier can be overcome by applying an ac signal at high frequencies. At low frequencies (e.g. 60 Hz) dc sputtering conditions occur and the cathode and the anode alternate at each half of the cycle. The frequency factor becomes effective above ~1 MHz [19]. In this range, the electrons oscillating back and forth by the electric field gain sufficient energy to ionize argon atoms. This is in addition to the acceleration away from the target. Since these field-driven electrons generate ions directly, sustaining the plasma does not rely on the secondary electrons emitted from the target. Even though the process seems symmetric considering the cycles, it is asymmetric due to the system geometry [20]. At radio frequencies, voltage can be coupled through any impedance, therefore the electrode resistivity does not matter and insulator materials can be used as target. Due to the lower discharges at the target, the rf sputtering yields deposition rates lower than dc sputtering [21].
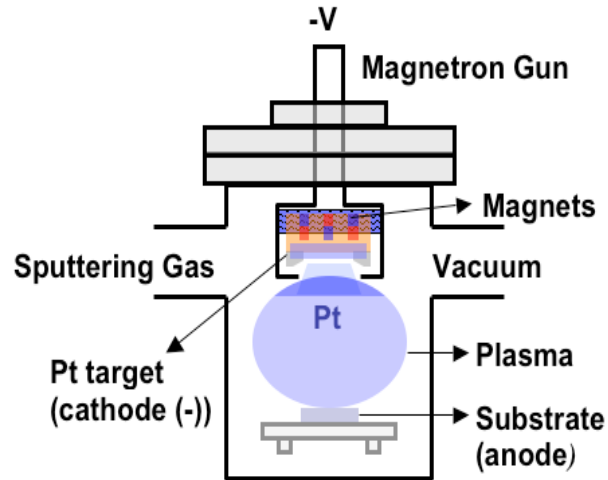
Figure 2.16 Schematic depiction of magnetron sputtering [21].

Thin film of metals and ceramics find a number of applications, such as corrosion resistant coatings, deposits on tectiles, decorative coating, catalysts, thermal sensing elements, semiconductor contacts, interconnect devices in integrated circuits, magnetoresistance sensors and magnetic storage media. Polycrystalline semiconductors find use as conducting elements in circuits and devices, optical interconnects, and as active elements in several semiconductor devices. Piezoelectric films in acoustic wave transducers, ferroelectric films for nonvolatile memories and high dielectric constant films for integrated circuits use polycrystalline films [12].

Many perovskite materials have attracted considerable attention for several decades because of their ferroelectricity, dielectrics, optical and electro-optic properties, and potential device applications including ferroelectric random access memories, electro-optic switches, and modulators. In contrast to bulk materials, the ferroelectric thin films are superior for increased speeds, reduced operating voltages, and enhanced efficiency [23]. There is a great need for high quality thin film ferroelectric materials for applications in thin film voltage tunable capacitors, frequency agile microwave components, and in computer memory elements. For room temperature operation, the ferroelectric material should have a Curie temperature that results in low loss, low leakage current, and a large change in relative dielectric (ϵ_r) with applied voltage

24

(tunability) [24]. Recently, the ferroelectric thin film optical devices are especially attractive because of their predominance for monolithic integration with electronic and optical electronic devices. As a typical ferroelectric material, BTO thin films have high optical transparency in the visible wavelength region, high refractive index, and low extinction coefficient, which have been used for integrated optic devices, such as optical memory, optical storage, low-voltage electro-optic switching, etc. Thus, it is interesting to investigate the optical properties of BTO and its doped materials [22,23]. Single crystals such as MgO, sapphire, $LaAlO_3$, and $SrTiO_3$ (STO) have been mainly used as substrates for the deposition of the BTO and its doped ferroelectric thin films in the applications of optical devices, as the epitaxial films grown on such single crystals have better optical properties than the polycrystalline films grown on quartz substrates. The uses of quartz as substrates have an economic advantage, as they are much cheaper than single crystals. Therefore, it is necessary to fabricate well-oriented BTO and its doped ferroelectric thin films on quartz substrates. However, the growth of perfect and pure ferroelectric crystals has proven to be very difficult [23]. Leng et al. [23] formed $Ba_xSr_{1-x}TiO_3$ (x=0.6 and 0.8) on indium-doped tin oxide (ITO) coated quartz substrates using radio-frequency magnetron sputtering. Sputtering conditions are provided in Table 2.2. The as-deposited BST thin films were annealed at 650 °C for 20 min in oxygen. In order to study the electrical properties of the BST thin films/ITO/quartz substrates, Pt was sputtered on the BST film as electrode to form a metal/BST/semiconductor configuration.

Table 2.2 Sputtering conditions for preparation of BST thin films [23]

Target diameter	120 mm
Target-substrate spacing	72 mm
Sputtering gas	Ar(80%)+O_2(20%)
RF power	95-100 W
Substrate temperature	400 °C
Gas pressure	0.12-0.14 Pa
Growth rate	0.9-1.2 nm/min

The crystalline structure of the BST films annealed at 650 ℃ for 20 min were characterized by XRD analysis (Figure 2.17). As can be seen, the highly (111)-oriented BST films are revealed. As the x-ray scanning pattern shows, $Ba_{0.6}Sr_{0.4}TiO_3$ films have a cubic structure characterized by appearance of (001), (101), and (111) peaks, whereas the $Ba_{0.8}Sr_{0.2}TiO_3$ films with the appearance of (001), (101), (111), and (002) peaks have pure tetragonal perovskite structure without a secondary phase.
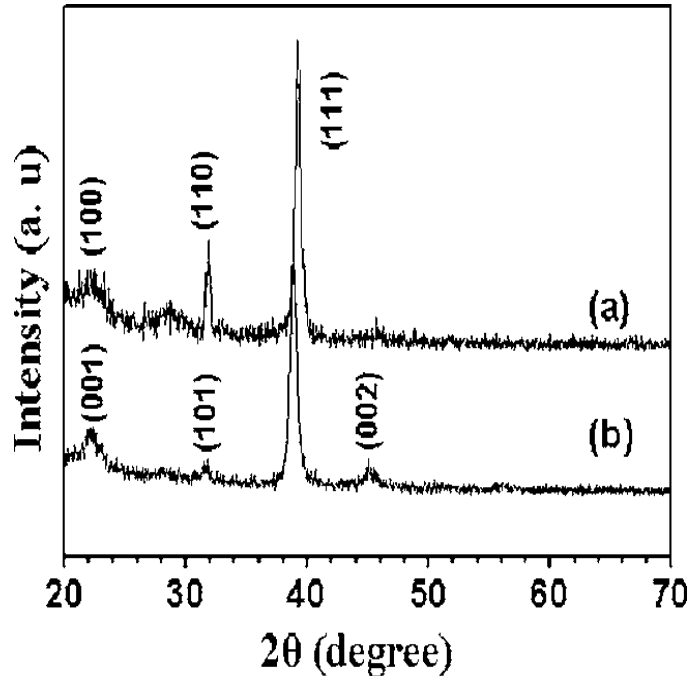
Figure 2.17 XRD pattern of the annealed BST thin films: (a) x=0.6 and (b) x=0.8 on ITO/quartz substrate. Annealing temperature is 650 ℃ [23].

Ferroelectric properties of BST thin films were measured in a metal/ferroelectric/semiconductor (MFS). A well saturated P-E hysteresis loop of $Ba_{0.8}Sr_{0.2}TiO_3$ thin film is shown in Figure 2.18. The remnant polarization (P_r) and coercive field (E_c) are approximately 6.75 µC/cm² and 43.2 KV/cm, respectively. The results show a good ferroelectric property of BST films deposited by magnetron sputtering method. Moreover, optical properties of the BST thin films are quite valuable for the fabrication of optical devices. The optical properties of the BST thin films with x=0.6 and 0.8 have been investigated in the 400–1020 nm wavelength region by spectroscopic ellipsometry. The refractive index *n* and the extinction coefficient *k* of the

BST films were obtained by fitting the model function to the experimental spectroscopic ellipsometric data. The results reveal that the extinction coefficient of the BST films is very small, showing that the BST films are highly transparent in the measured wavelength region [23,25].
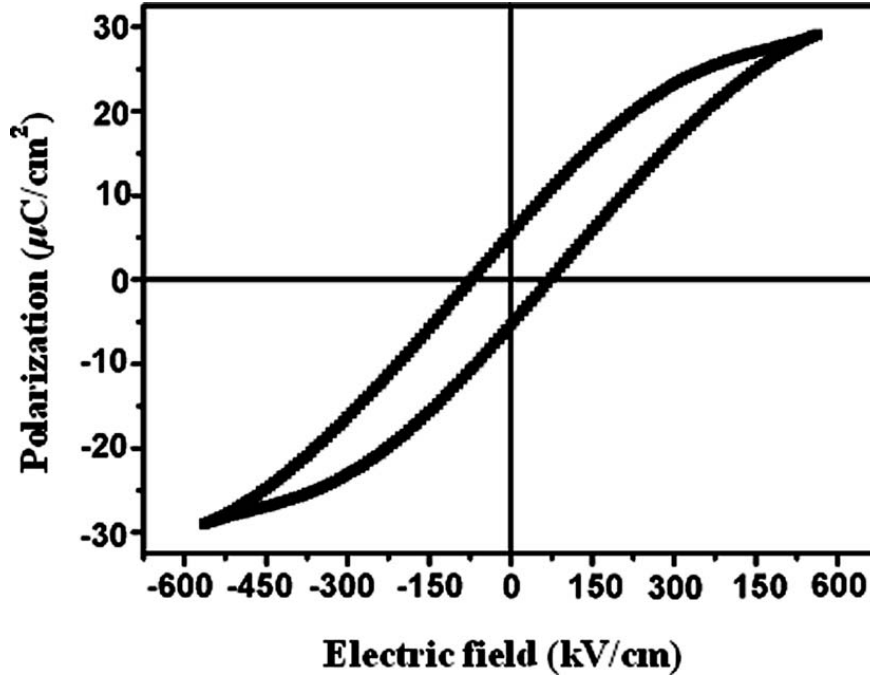
Figure 2.18 Polarization-electric field hysteresis loop of the $\mathbf{Ba_{0.8}Sr_{0.2}TiO_3}$ thin film [23].

BST can also be deposited by off-axis cosputtering targets of STO and BTO. Cukauskas et al. [24] deposited the films on (100) MgO and LaAlO$_3$ substrates at 550 ℃ and at argon/oxygen (3:1) gas pressure of 20 Pa. Reaction of the sputtered species in the plasma resulted in the growth of Ba$_{0.5}$Sr$_{0.5}$TiO$_3$ films. The film composition can be set by the relative power levels of the STO and BTO targets. The thin film growth process was done in several steps or layers. This was accomplished by interrupting the deposition, cooling the substrates in oxygen, and removing any particulates from the film surface with dry nitrogen gas. Successive deposited layer proceeded with identical conditions to the first and concluded with cooling the films in one atmosphere of oxygen before removing them from the vacuum chamber. The films were annealed in a tube furnace in one atmosphere of flowing oxygen at 780 ℃ for 8 h. The cosputtered films were compared with deposited films by off axis sputtering of single Ba$_{0.5}$Sr$_{0.5}$TiO$_3$ target

with the same parameters of temperature and pressure. A diffraction pattern of BST on MgO is illustrated in Figure 2.19. The x-ray peak positions correspond to polycrystalline BST dominated by the (h00) reflections. Diffraction peaks for BTO and STO are not observed in these films. Similar diffraction spectrum but more (h00) oriented were observed for the films on LAO.
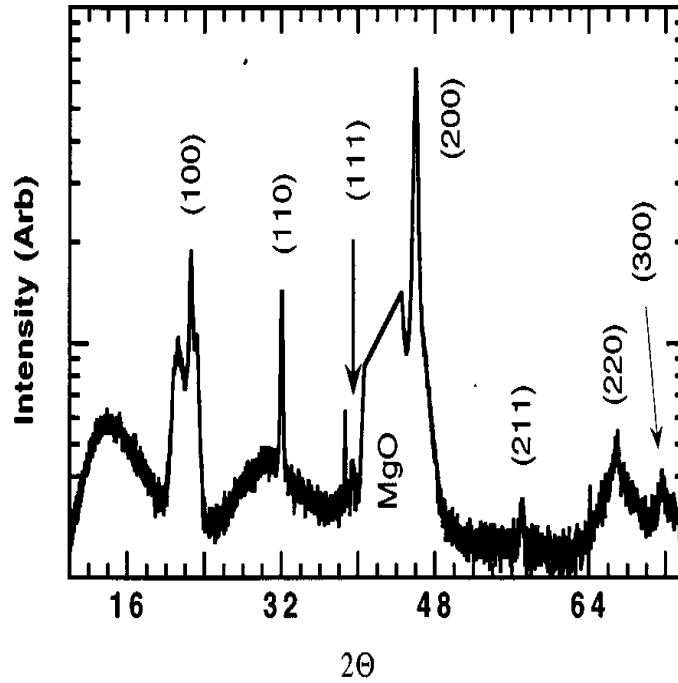
Figure 2.19 The x-ray spectrum of a BST film deposited at 550 °C on MgO and annealed at 780 in flowing oxygen for 8 h. The BST peaks are indexed and the MgO °C substrate peak has been suppressed [24].

The films were processed into arrays of interdigitated capacitors in order to measure the capacitance and loss characteristics at microwave frequencies [26]. Figure 2.20 illustrates the capacitance of device (Q) versus frequency for the indicated value of bias voltage. The capacitance and hence the dielectric constant is relatively small compared to similar structure fabricated from PLD films, which is associated with either small grain size and/or operation significantly above the Curie temperature of the films [25,26].
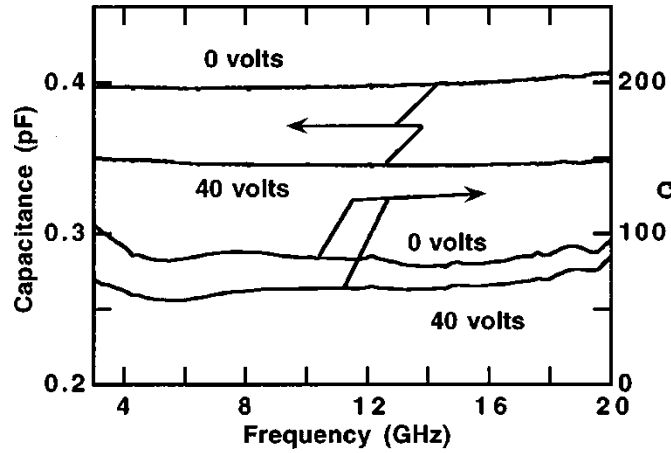
Figure 2.20 The plot of capacitance and Q for a MgO based BST film having one interface layer. The characteristics are illustrated for the two bias value indicated [25].

The capacitance versus bias voltage at 10 GHz is illustrated in Figure 2.21. The hysteresis is a measure of the polarization of the BST film. The scope of the curve at ± 40 V indicates that further tuning is available at higher voltage.
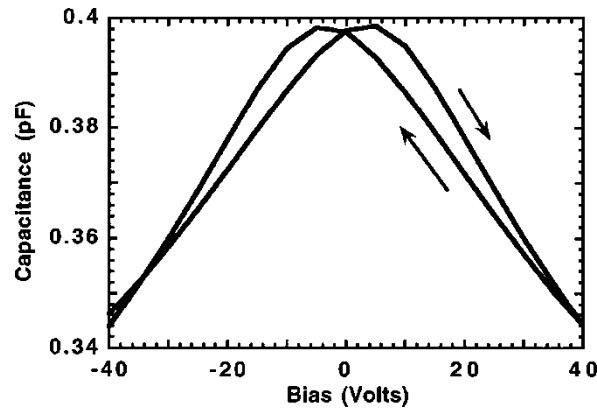
Figure 2.21 The capacitance as a function of bias voltage at 10 GHz for the device whose data is illustrated in the previous figure. The hysteresis is a measure of polarization of BST film [25].

The electrical characteristics from 50 MHz to 20 GHz were determined for interdigitated capacitors fabricated from the films. There was a trade-off between Q and tuning for devices on both MgO and LAO substrates. Films were made with an interface within the interior of the film which amounted to a seed layer and resulted in lower loss for films grown on MgO. The best Q observed was beyond the measurement capabilities

29

of the instrument/device system and was estimated to be greater than 1000 and the device had a tuning slightly above 2%. This film had a seed layer close to the MgO substrate. Capacitors fabricated from films made from a single BST target using similar deposition parameters had greater tuning and lower device Q characteristics than the cosputtered BST films. Off-axis cosputtering from STO and BTO targets is a growth technique which has good potential in meeting the film quality specifications for many ferroelectric thin film applications.

2.4 Deposition of Barium Titanate on Nickel Substrate

Due to excellent piezoelectric properties of barium titanate, BTO thin films have been deposited on various substrates using a broad spectrum if techniques to provide a platform for many device applications, such as ferroelectric radom access memories, optical modulators, waveguides, and microelectromagnetic systems [27]. Unique properties of BTO thin films, such as excellent piezoelectric properties similar to its single crystal ferroelectrics, enable it to be a great candidate for the development of the unobtrusive piezoelectric wafer active sensor arrays for structural health monitoring [28]. However, major challenges exist in extending this technology to structural health monitoring since the fabrication of the ferroelectric thin films of BTO on structural materials (steel, nickel, aluminum, etc.) has not been attempted yet, which will raise a number of crystallinity and interface-related challenges. Yuan et al. [29] have used pulsed laser deposition to achieve *in situ* fabrication of BTO thin films on the typical structural material Ni, facilitated by an unltrathin interfacial buffer layer NiO. NiO has a rocksalt structure with an excellent electrical conductivity and chemical stability, which can be used as conductive electrode and as the barrier for blocking the interdiffusion or inter-reaction between the ferroelectric film and metal substrate. Also, socksalt structure of NiO has good crystallographic compatibility to the perovskite microstructure of BTO, which facilitates film growth by bonding the BTO layer onto the Ni substrate.

Microstructure studies reveal that the as-deposited BTO films have a nanopillar structure. Transmission electron microscopy (TEM) studies of BTO/Ni interface have demonstrated that the BTO/NiO/Ni layered films have sharp interfaces with no

interdiffusion or reaction. Figure 2.22 shows the TEM characterization of BTO thin film on Ni substrate.
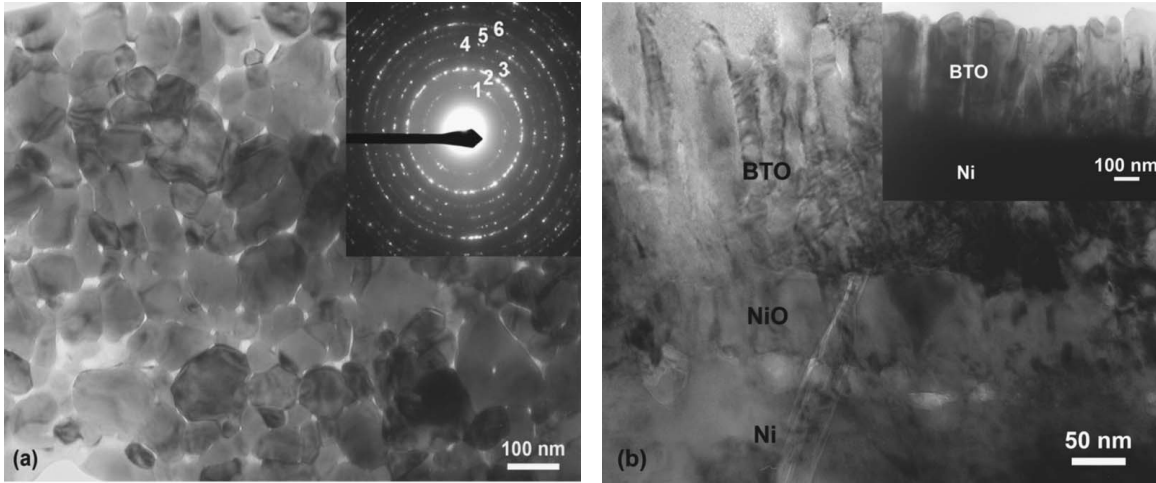
Figure 2.22 (a) Plan-view TEM with the inset electron diffraction pattern of BTO film and (b) Cross-sectional TEM of BTO/Ni (with the inset of a low magnification image) showing the nanopillars and interface structure [29].

Ferroelectric polarization measurements have shown the hysteresis loop at room temperature in the film with a large remanent polarization, indicating that the ferroelectric domains have been created in the as-deposited BTO films. The polarization response of this film was surprisingly found to be about 30% larger than that of BTO single crystalline and polycrystalline bulk materials [30]. Frey et al. [31] asserted that such a large piezoelectric response is due to the uniform nanodomain structure.

Jiang et al. [32] fabricated the orientation-preferred structures of ferroelectric BTO thin films on Ni substrate using pulsed laser ablation. In order to do so, a layer of NiO with the thickness of 50 to 80 nm was synthesized via in-situ oxidation treatment as an interlayer between Ni substrate and BTO. The BTO films have nanopillar, crystalline tetragonal structures with a good interface with respect to the substrate. More than 60% of BTO grains share a common orientation with their a-axis in the film plane and the [011] direction parallel to the growth direction of the films. As Figure 2.23 shows, this orientation-preferred nanopillar structures were grown on a layer of nanocrystalline Ni. The cross-sectional TEM image shows that BTO film has a thickness of about 200 nm and consists of nanopillar structure with lateral dimensions of about 100 nm, ehich is

close to the value obtained from the plan-view TEM. The intermediate (IM) layer between BTO film and Ni substrate shows nanocrystalline structure. Figure 2.23(b) is a plan-view TEM image and the SAED pattern of the IM layer, in which the nanostructures show different characteristics from that shown in Figure 2.23(a). The grain size of nanostructure varied from 30 to 100 nm in diameter and is smaller than that of the BTO grains. The nanostructure in IM layer were found to be pure Ni (fcc, a=3.52 Å) as idendified by the electron diffraction analysis. Diffraction rings 1, 2, 3, and 4 have a lattice spacing of 2.03 Å, 1.76 Å, 1.25 Å, and 1.06 Å, respectively, which can be identified as the (111), (200), (220), and (311) reflection of Ni.
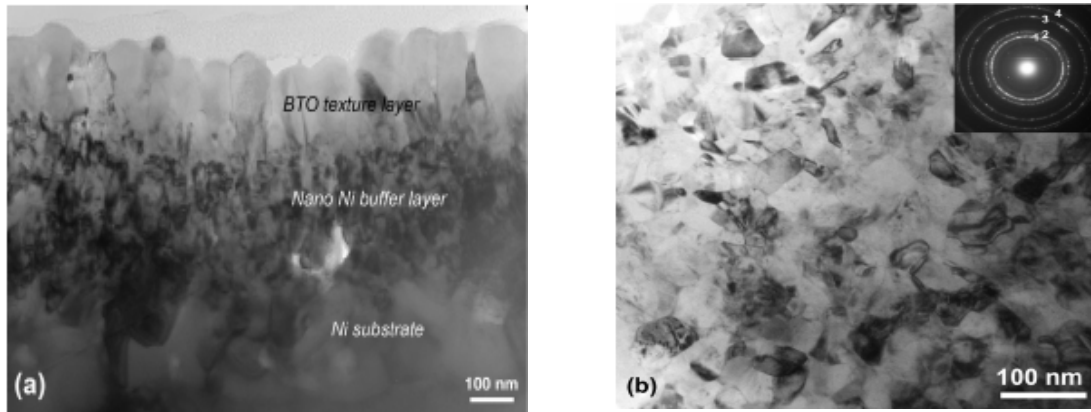
Figure 2.23(a) Cross-section TEM of BTO/Ni showing film and interface structure and (b) Plan-view TEM image and SAED pattern (inset) of the intermediate layer in (a) [11].

The observation of nanostructured pure Ni intermediate layer is different from the NiO layer that was synthesized prior to the deposition of the BTO films. Such difference can be understood by looking into the entropy and the free energy of BTO and NiO. Since entropy and free energy of NiO are higher than those of BTO, it can be speculated that during the deposition, oxygen atoms in the NiO intermediate layer migrated to the BTO film layer.

2.5 Deposition of Nanocrystalline Nickel on Bulk Nickel Substrate

Nanocrystalline materials have been subject of intensive research in recent years because of their unique properties and applications in science and technologies. They are characterized by crystallites with a grain size less than 100 nm and a high volume fraction of the grain boundary, which may comprise as much as 50% of the total crystal volume. Corrosion performance of nc-metals and alloys received a considerable attention during the past two decades. These reports have demonstrated that the effect of nano-structuring on corrosion behavior varies among metal systems and corrosion environments; hence, it is difficult to predict the electrochemical behavior of nc-metals from the known properties of their coarse-grained polycrystalline analogues. In comparison with conventional coarse-grained pure metals, the general corrosion resistance of nc-counterparts was mostly decreased, while they showed higher resistance to localized intergranular corrosion because the corrosion pits are distributed uniformly due to an increased volume fraction of the grain boundaries [33].

Nickel is mostly used in structural alloys, either as alloy based, e.g. in nickel-based alloys, or as an alloying element, for example in austenitic stainless steels. Comparisons of electrochemical corrosion of nc-Ni with conventional coarse-grained Ni were studied by several investigators. Rofagha et al. [34] have reported that 32 nm-grained Ni exhibited a higher passive current density in de-aerated 1 M H_2SO_4 compared with coarse-grained ($100 \ \mu m$) polycrystalline Ni. Mishra et al. [35] have also investigated the electrochemical and corrosion behavior of nc-Ni of different grain sizes (8-28 nm) in 1 M H_2SO_4. They reported that the passive current density for nc-Ni was higher than that for bulk Ni because of the defective nature of passive film on nc-Ni, while the breakdown potential for nc-Ni was higher than that for coarse-grained polycrystalline Ni. However, they reported that the corrosion rate of freshly exposed nc-Ni was lower compared to bulk Ni, indicating a higher hindrance to anodic dissolution from the nc-Ni surface.
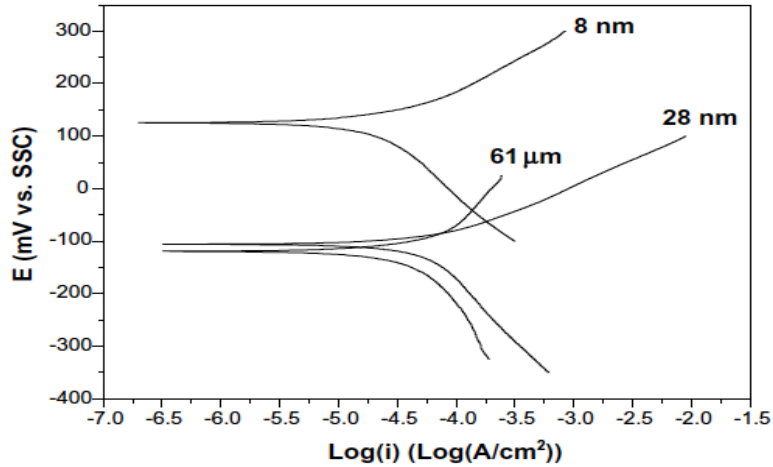
Figure 2.24 Tafel Plot for bulk Ni, 28 and 8 nm grain sized nanocrystalline Ni conducted in 1 M H_2SO_4 at a scan rate of 0,5 mV/s. The experiments were conducted immediately after immersion of the samples in the electrolyte [35].

The higher breakdown potential of the nc-Ni coatings compared to microcrystalline counterparts in 3.5% NaCl solution was reported by Raeissi and co-workers [36]. However, they observed that in the case of nc-deposits, coatings with higher grin size showed higher resistance to pitting corrosion. Zhao et al. [37] have investigated the corrosion resistance of nc-Ni in 3.5% NaCl solution with the grain size ranging from 30 to 56 nm. They did not observe the clear dependency of corrosion resistance on the grain size; the 49 nm-grained specimen showed the highest corrosion resistance, while the lowest corrosion resistance showed 56 nm-grained Ni specimen. Wang et al. [38] have investigated the effect of grain size reduction on the electrochemical corrosion behavior of nc-Ni in alkaline solution (10% NaOH). They have reported that the corrosion resistance gradually increased with the grain size reduction from 3 μm to 16 nm due to the faster formation of continuous Ni hydroxide passive films at surface crystalline defects and the relatively higher integrity of passive films.

Nanocrystalline nickel and nickel alloy coatings prepared by dc magnetron sputtering deposition method are very interesting materials due to their enhanced mechanical, catalytic, and corrosion properties [39].

Corrosion resistance of alloys depends not only on their composition, but also on their microstructure. Nanocrystallization of Ni-based superalloys has been found capable

34

of enhancing their high-temperature oxidation resistance, because of easier formation of protective oxide layer. Liu et al. [40] studied electrochemical corrosion behavior of Ni-based superalloy nc coatings in 0.5 M NaCl + 0.05 M H_2SO_4 solution with grain size of 10 nm, 50 nm, and 100 nm, which was fabricated by magnetron sputtering. Their results indicate that a n-type semicondutive passive film with porosity and incorporation of chloride ions formed on the nc coating with 100 nm grain size, which increased the susceptibility to pitting corrosion. The nc coating with 10 nm and 50 nm grain size formed compact, non-porous, and p-type passive films without chloride ions, which improved resistance to pitting corrosion. Potentiodynamic polarization curves for three coatings are shown in Figure 2.25. All coatings could be passive under suitable potential. The breakdown potentials for the three coatings are similar, but minimum passive current density decreased by decreasing grain size. Above 0.4 V, the passive current density of NC-3 with 100 nm grain size slightly increased with potential. They concluded that the smaller grain size of materials decreases the amount of chloride ions adsorbed on the surface and promoted the formation of compact passive film, which significantly increased the material's resistance to pitting corrosion in acidic solutions.
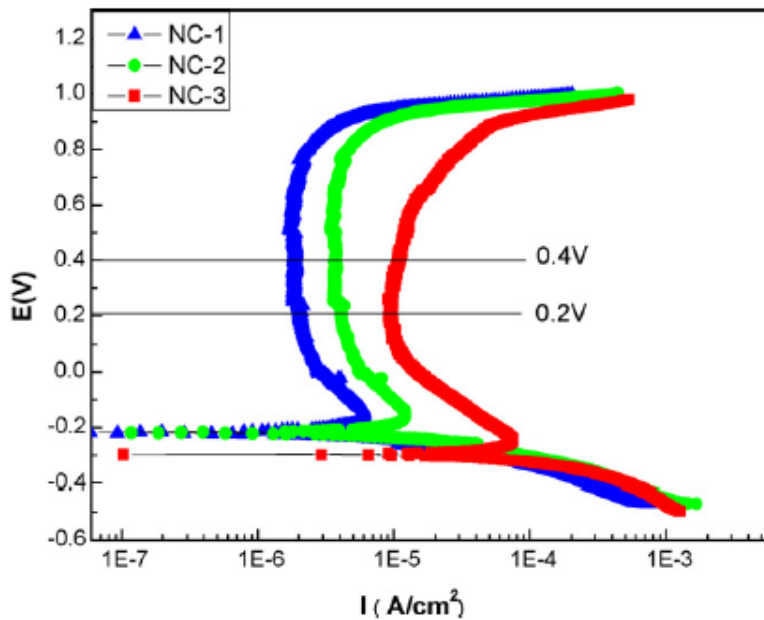
Figure 2.25 Potentiodynamic Polarization plots of the NC-1, NC-2, and NC-3 with 10 nm, 50 nm, and 100 nm respectively, in 0.5 M NaCl + 0.05 M H_2SO_4 [40].

Geng et al. [41] studied the oxidation behavior of nc-Ni coating, deposited on pure Ni substrate via magnetron sputtering, in air at 700-900 ℃. They reported that nanocrystallization of pure Ni promoted oxidation during early stage. After that, oxidation rates are about the same in samples with or without the nanocrystalline layer.

Hugo et al. [42] compared tensile properties of two nanocrystalline Ni thin films, one prepared via DC magnetron sputtering and the other prepared via Pulsed Laser Deposition (PVD), by straining them in-situ in the TEM. Although the grain sizes were similar, the two films behaved quite differently under tension. Figure 2.26 shows an image of an area immediately ahead of a growing crack in the PVD film. Dislocation arrays (multiple dark lines within a grain) were positively identified from dynamic sequences and are indicated with black arrows. Grain boundary thinning and cracking (white arrows) might be seen at light edges of grains. Figure 2.27 shows an image of a growing crack in the DC Magnetron Sputtered film just before the crack jumping several micrometers. Dislocation arrays, some of which were identified dynamically, are indicated with arrows. This micrograph shows that thinning ahead of the crack tip was discontinuous from one grain to the next, indicating that slip transfer was highly limited. This study showed that the sputtered nc nickel film was found to behave in a brittle manner, with failure occurring via rapid coalescence of intergranular cracks. Conversely, the laser deposited film behaved in a ductile manner, with failure occurring by slow ductile crack growth. The difference in failure mechanism was attributed to presence of grain boundary porosity in the sputtered thin film.
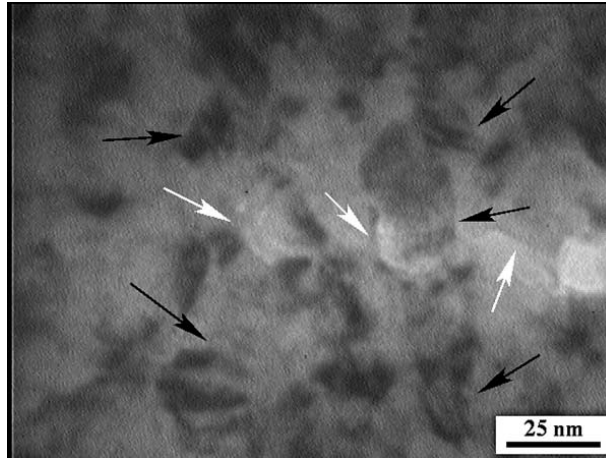
Figure 2.26 video image of an area immediately ahead of a growing crack in the PLD film [42].
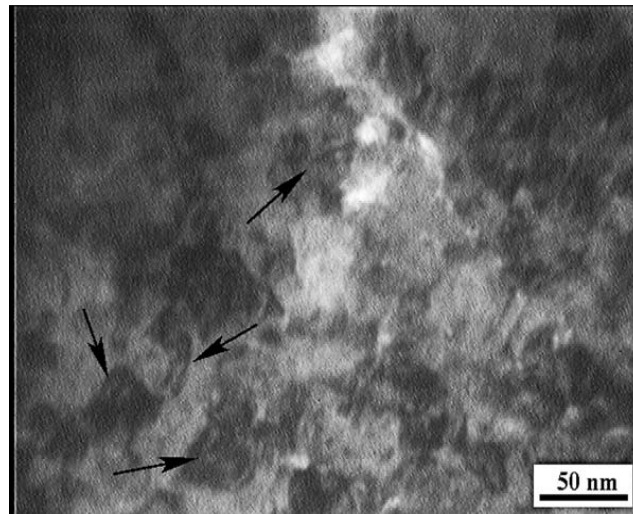
Figure 2.27 video image of a growing crack in the DCMS film [42].

Nanocrystalline materials often exhibit ultrahigh strength, which is suitable for potential engineering appications. However, some experiments showed that those high-strength nc metals are of very low ductility or even brittle [43-44]. Since strength and ductility are of the two most important mechanical properties of any material, numerous studies have been conducted to understand the deformation mechanism and the fracture behavior of nc metals. Earlier reports on nc metals show that the low ductility seems to be attributed to the pre-existing flaws, which generally would induce a catastrophic

failure during deformation. Recent defect-free bulk samples, especially those fabricated by electro-deposition and severe plastic deformation (SPD), do exhibit a ductile behavior, but they are very susceptible to the plastic instability in tension, i.e. early cracking [45]. The local shear band is often observed on the deformed surface of these nc metals. The plastic instability in the form of shear band has been proposed to be related to the low strain hardening capacity and sourced from the insufficient dislocation activities in the nc grains [45,46]. Thus, some strategies such as, the twins or micrometer-sized large grains into the matrix with fine nc grains, were recently taken to tackle the plastic instability of these materials [47]. However, all these results are related to the nc materials with an average grain size of 25-100 nm (experimentally feasible region).

Recent atomic simulations have indicated that as the grain size falls into the lower nano regime of ~25 nm, especially less than the so-called critical value (e.g., 18 nm for Al and 14 nm for Cu), the dislocation based mechanism would be suppressed and novel mechanisms such as Grain Boundary (GB) sliding or grain rotation could contribute to the plasticity [48]. Such transition in the deformation mechanism is implied by the observed breakdown of Hall-Petch scaling at the grain size below about 20 nm (Figure 2.28).
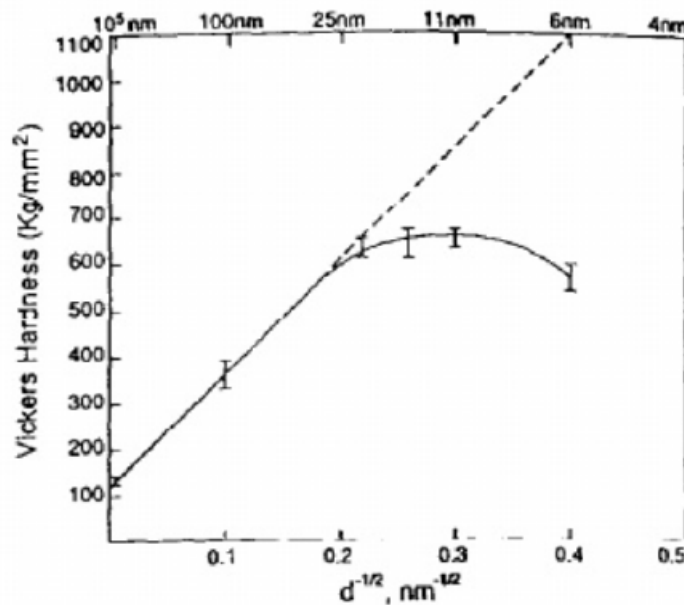
Figure 2.28 Hall-Petch plot for electrodeposited nickel [49].

38

Shen et al. [50] studied the deformation and fracture behavior of electrodeposited nc Ni, with average grain size of 19 nm and thickness of 5.4 mm, under compression. According to their studies, nc Ni exhibited a high strength of 2920 MPa and an accepted good ductility of 16%. A novel fracture character, i.e., the triple-junction shaped micro-cracks with the size varying from a few to several tens of micrometers which run through the holistic fracture body of the nc Ni, was observed (Figure 2.29).

The reason for formation of such cracks is attributed to GB activities, which leads to the formation of nano-sized void, and the subsequent formation of micro-cracks.
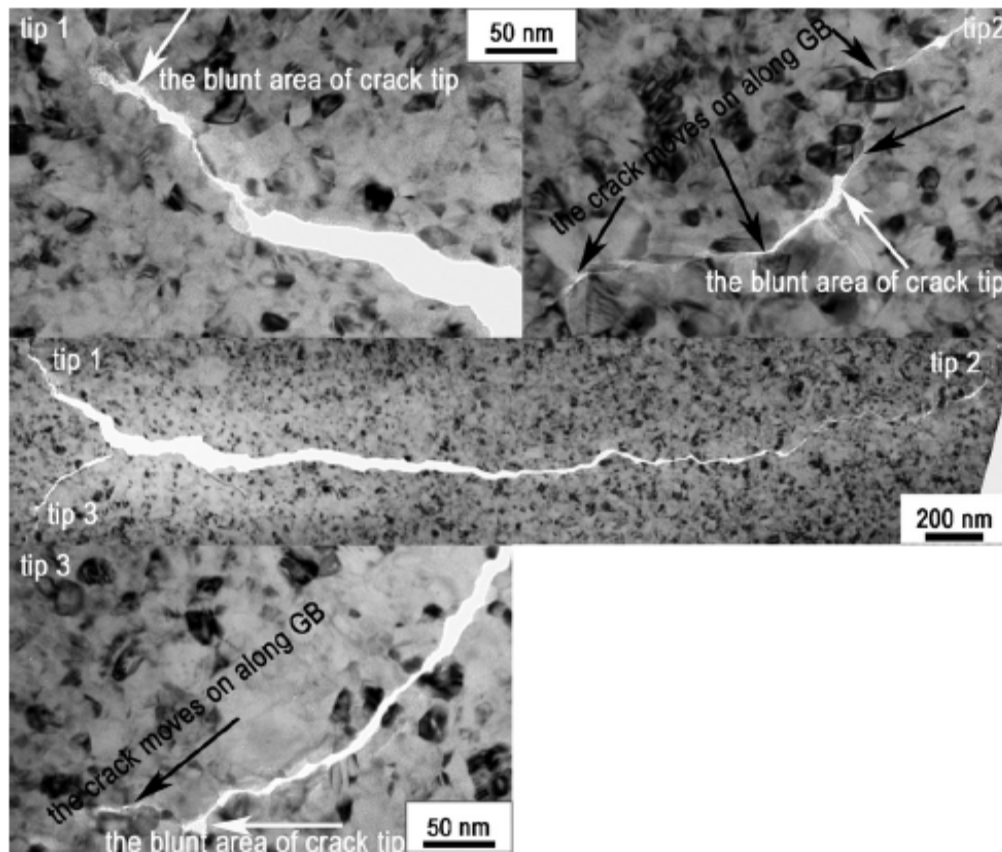
Figure 2.29 The TEM micrograph of the captured area with trifurcate-shape microcrack in the non-fracture nc Ni specimen subjected to a compressive strain of 14% [50].

Chapter 3

THIN FILM SYNTHESIS AND CHRACTERIZATION

Barium titanate thin films were fabricated on bulk nickel 200 and silicon wafer substrates using RF magnetron sputtering, which was conducted in a home-made hybrid plasma assisted system. In order to deposit barium titanate on nickel, two different interlayers were used; nickel oxide and nanocrystalline nickel. Nanocrystalline nickel was fabricated on bulk nickel using the same sputtering system by utilizing DC power, and nickel oxide was synthesized by oxidizing nickel substrate in a tube furnace in air. Synthesized samples are introduced in Table 3.1.

Table 3.1 Synthesized Samples

Sample #	Substrate	Interlayer	Coating	Interlayer Fabrication Method
1	Ni 200	nc Ni	BTO	DC magnetron sputtering
2	Ni 200	NiO	BTO	Tube furnace
3	Si Wafer	nc Ni	BTO	DC magnetron sputtering
4	Si Wafer	nc Ni	BTO	DC magnetron sputtering

The details of the deposition conditions for each film are discussed in this chapter. The microstructure of thin films was characterized using XRD, TEM, and AFM.

3.1 Magnetron Sputtering System

The deposition of barium titanate and nanocrystalline nickel films was conducted in a home-made hybrid plasma assisted sputtering system at the Surface and Nano Engineering Laboratory (SANEL). As demonstrated in Figure 3.1, this system mainly consists of a cylindrical stainless steel chamber, RF and DC power supplies, and electronic controllers. The cylindrical chamber is 47 cm in diameter and 50 cm in height

and contains three 2-inch diameter guns mounted to the bottom plate The front gun has a high magnetic source, and other two guns are equipped with low strength magnetic sources. Each gun can be easily connected to DC or RF power supplies. The guns are positioned to have a 30° inclination to the substrate holder center. The sputtering target holder and substrate holder have a face-to-face arrangement with an adjustable distance between 100-150 mm. The magnetron guns are able to support targets with thickness of 0.125, 0.185, or 250 inch. Targets can be shielded by a pneumatic shutter above each gun. The sample holder and the magnetron guns are shown in Figure 3.1.
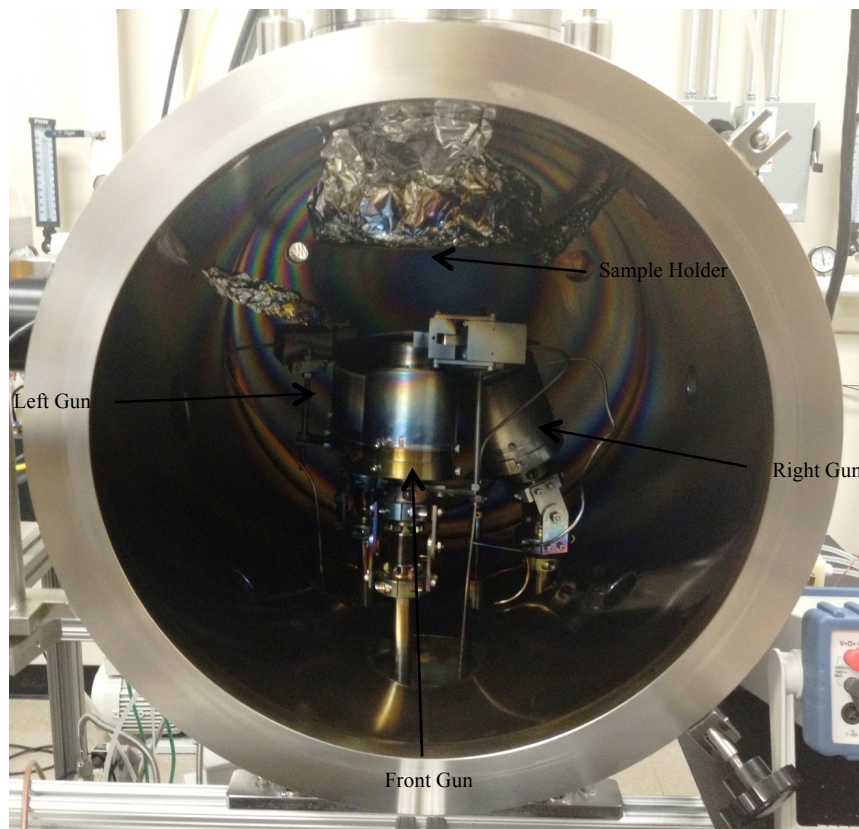
Figure 3.1 Magnetron Sputtering Chamber.

RF power is provided by an AJA Seren RF generator and manual matching network, while DC power supplier is made by Glassman High Voltage Inc, series EK. The substrate can be heated up to 850℃, controlled by an AJA SHQ-15 unit and a thermal couple connected to the substrate holder. Samples can be mounted to and held by the substrate holder, which is a 10 cm diameter plate and has rotation capability. The

substrate can be RF or DC biased up to 50 W and 1000 V, respectively. The deposition chamber is connected to a mechanical roughing pump and a cryopump to obtain and keep high vacuum down to 1×10^{-8} Torr. During the deposition, a MKS 146C PID controller maintains a very precise pressure inside the chamber by controlling an automatic gate valve. All magnetron guns and substrate holder are cooled circularly using a Thermo Scientific NESLAB RTE 740 water chiller to avoid heating damage to guns and maintain the deposition temperature stable on the substrate. Argon gas flows to the chamber to start and preserve the plasma, controlled by a Unit Instrument mass flow controller to meet the required pressure during deposition. Prior to any deposition, a DC power provided by Advanced Energy DMX-1K is used to clean the substrate. The power supplies are shown in Figure 3.2.

Figure 3.2 Magnetron Sputtering System Power Sources and Controllers.

3.2 Tube Furnace

In order to oxidize nickel disk samples and grow a layer of nickel oxide, the sample was placed in a Thermolyne 79300 tube furnace. This furnace consists of a single heated zone split with size of 24 in or 60 cm and maximum temperature of 1200℃. There is built-in temperature controller, which conserves valuable bench space. The exposed coil heating elements are embedded in ceramic fiber insulation and provide heating rate of $1\,^{\circ}C/_{S}$. In order to provide a desired atmosphere at high temperature, gas can be supplied into the tube.

To fabricate NiO layer, the furnace temperature was raised to 750℃ and a nickel disk sample was placed at the middle of the tube. After 1hr, sample was extracted and cooled in the air.

Figure 3.3 Thermolyne 79300 Tube Furnace.

3.3 Sputtering Targets and Deposition Conditions

A nanocrystalline nickel interlayer was sputtered on bulk 200 nickel discs and samples of silicon wafer. Nickel discs were 2 cm in diameter and 2 mm in thickness, while the silicon wafer substrates were 2 cm × 2 cm × 300 μm. Deposition was conducted in the hybrid plasma assisted sputtering system, using a 99% pure nickel target with diameter of 5 cm and thickness of 0.63 cm. The deposition conditions are listed in Table 3.2.

Table 3.2 Sputtering Condition for Deposition of nc-Ni

Gun	High Magnetic Power (right gun)
Gun-substrate Distance	110 mm, 19.5°
DC Power	150 W
Voltage	310 V
Current	530 A
Gas	Ar
Gas Pressure	10 mTorr
Flow Rate	30 sccm
Temperature	RT
Deposition Time	1 hrs
Substrate Bias	None
Substrate Rotation	20 rpm

Prior to film deposition, substrate cleaning was carried out using Ar^+ plasma. The sputtering chamber was pumped down to 25 mTorr, using the mechanical pump, and then down to 10^{-7} Torr using the cryopump. The Ar gas flow was controlled at 10 sccm. The substrate samples were cleaned by Ar^+ plasma using 30 W DC power at room temperature for 10 min.

Nickel oxide was synthesized by oxidizing nickel substrates in the tube furnace in air. Samples were held in the furnace at 750℃ for 1 hour (Sample# 2).

Barium Titanate was deposited on all four samples using the hybrid plasma assisted sputtering system. The BTO target was 99.9% pure with the same size as nickel target (5 cm diameter and 0.63 cm thickness), which was purchased from Kurt J. Jesker company.

The deposition condition for BTO sputtering is provided in Table 3.3.

Table 3.3 Sputtering Condition for Deposition of BTO

Samples # 1, 2, 3		Sample # 4	
Gun	High Magnetic Power (front gun)	Gun	High Magnetic Power (front gun)
Gun-substrate Distance	80 mm, 19.5°	Gun-substrate Distance	80 mm, 19.5°
RF Power	100 W	RF Power	100 W
Voltage	120 V	Voltage	140 V
Current	500 A	Current	540 A
Gas	Ar	Gas	Ar
Gas Pressure	20 mTorr	Gas Pressure	20 mTorr
Flow Rate	30 sccm	Flow Rate	30 sccm
Temperature	350℃	Temperature	800℃
Deposition Time	3 hr	Deposition Time	2 hr
Substrate Bias	None	Substrate Bias	None
Substrate Rotation	20 rpm	Substrate Rotation	20 rpm

Before deposition of BTO, samples # 1, 2, 3 were cleaned by Ar^+ plasma using 30 W DC power at room temperature for 10 minutes.

In order to synthesize sample # 4, Ni and BTO targets were placed in the chamber at the right and front guns, respectively. The silicon wafer substrate was cleaned by Ar^+ plasma using 30 W DC power at room temperature for 10 min. Afterward, nc-Ni was

deposited for 1 hour with the same conditions mentioned in Table 3.2. In order to deposit BTO, the substrate temperature and chamber pressure were increased to 800℃ and 20 mTorr, respectively. After deposition, all the samples were cooled inside the chamber.

Table 3.4 presents the physical properties of bulk nickel, nanocrystalline nickel, and barium titanate as a reference.

Table 3.4 Physical Properties of Deposited Nickel and Nickel Oxide

Chemical Formula	Crystal Structure	Melting Temperature (K)	Density (g/cm^3)	Lattice Constant (Å)	Lattice Misfit with BTO (%)
nc-Ni	FCC	1726	8.90	3.520	14.20
NiO	FCC	2228	6.67	4.177	-3.76
BaTiO$_3$	Cubic	1891	6.06	4.020	--

3.4 Thin Film Characterization Techniques

3.4.1 XRD

The crystalline structure and grain size of the synthesized films were studied using a Siemens D500 X-ray diffractometer. A Cu Kα radiation source with the wavelength of 1.54056 Å was used at an accelerated voltage and filament current of 40 kV and 30 mA, respectively. Low angle scans were preformed with sample angle fixed on θ = 5°. The Scherrer equation was used to calculate the grain size of each material, considering the full width half maximum (FWHM) and diffraction angle (θ) of the related peak.

3.4.2 AFM

The surface morphology and roughness of deposited films were characterized using a NAVITAR N9457A AFM. The electrical properties and piezoelectric response of the BTO films were also studied using this AFM system.

3.4.3 High-resolution TEM

A Hitachi H-9500 high-resolution TEM operated at 300 kV with a point-resolution of 1.8 Å was used to study the microstructure of the samples. The cross-section TEM observation provided detailed information of the interface between the substrate and the deposited thin films, as well as the effect of interlayer deposited material. TEM micrographs demonstrate the BTO film nucleation mechanisms, growth, and a perspective of thin film-interlayer adhesion. Since making cross-section TEM samples from a nickel disk substrate is a difficult and sophisticated task, TEM analysis was preformed on samples with silicon wafer substrates.

3.4.4 Cross-section TEM sample Preparation

Cross-section TEM sample preparation incudes several basic steps as is illustrated schematically in Figure 3.4.

1. Cut a 3×3 mm rectangular piece from sample and the same size of silicon wafer using a diamond saw.

2. Glue these two as-cut slides face-to-face, using M-bond 610 adhesive.

3. Polish the cross-section side of glued samples on diamond lapping films of 30 μm, 3 μm, and 5 μm.

4. Mount the polished surface of sample on a 3 mm copper ring and grind the other side of it using a 1000 grit sand paper to reduce the thickness of sample to $10 - 20$ μm.

5. Place the sample on a precise sample dimple grinder and polish the sample using copper wheel and fine diamond paste.

6. In order to reduce the sample thickness, utilize a Ar-ion mill

system called Gatan 691, which is a precise ion polishing system (PIPS), until a there is a hole produced close to the film area. The edges of this hole could be thin enough for TEM analysis.
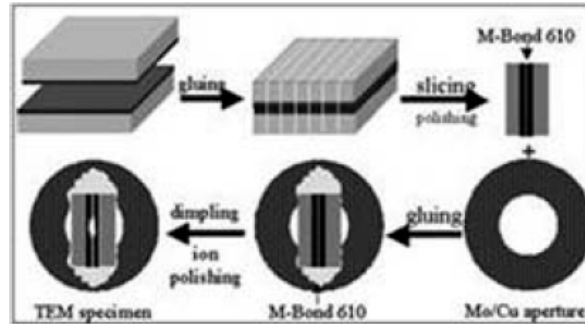

Figure 3.4 Schematic Illustration of Basic Steps for Cross-section TEM Preparation [51].

Chapter 4

RESULTS AND DISCUSSION

BTO is one of the most important ferroelectric pervoskite materials due to its excellent dielectric, ferroelectric, piezoelectric, and nonlinear optical peroperties in capacitors, antennae, storage and electro-optical devices. In order to have efficient devices, BTO in most of its applications, is required to be fabricated in thin film form with long-range structural coherence, high crystalline quality, and smooth surface. BTO has been deposited on various substrates by different methods, including chemical vapor deposition and molecular beam epitaxy. Among all the deposition methods, RF magnetron sputtering is becoming very important. Its capacity of depositing thin films over a large substrate area, as well as its low cost, simplicity and reproducibility has made this method very significant and applicable.

Typically, BTO has a cubic perovskite structure at temperatures above its ferroelectric curie point ($\sim 130°C$) with Ba at the cell corners, Ti in the body center, and O at the face centers and a tetrahedral structure ($a = 3.993$ Å, $c = 4.034$ Å) with Ti shifting from the center position, resulting in a permanent polarization of the structure along its c-axis. Figure 4.1 and Figure 4.2 show crystalline structure of BTO and its temperature dependency, respectively.
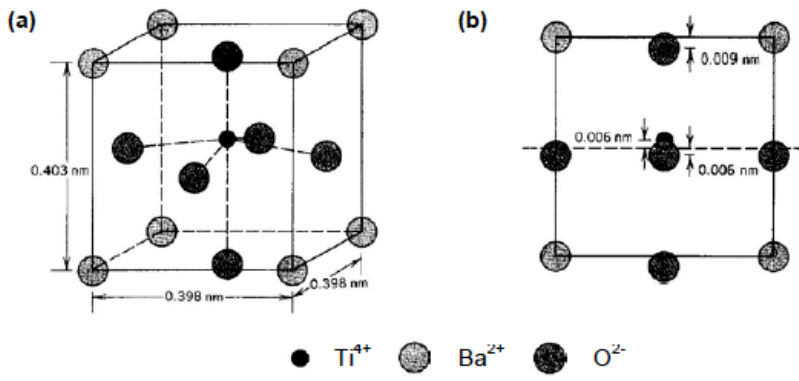
Figure 4.1 (a) Barium titanate ($BaTiO_3$) unit cell and (b) {100} projection showing the displacement of Ti and O from the center to the face [52].
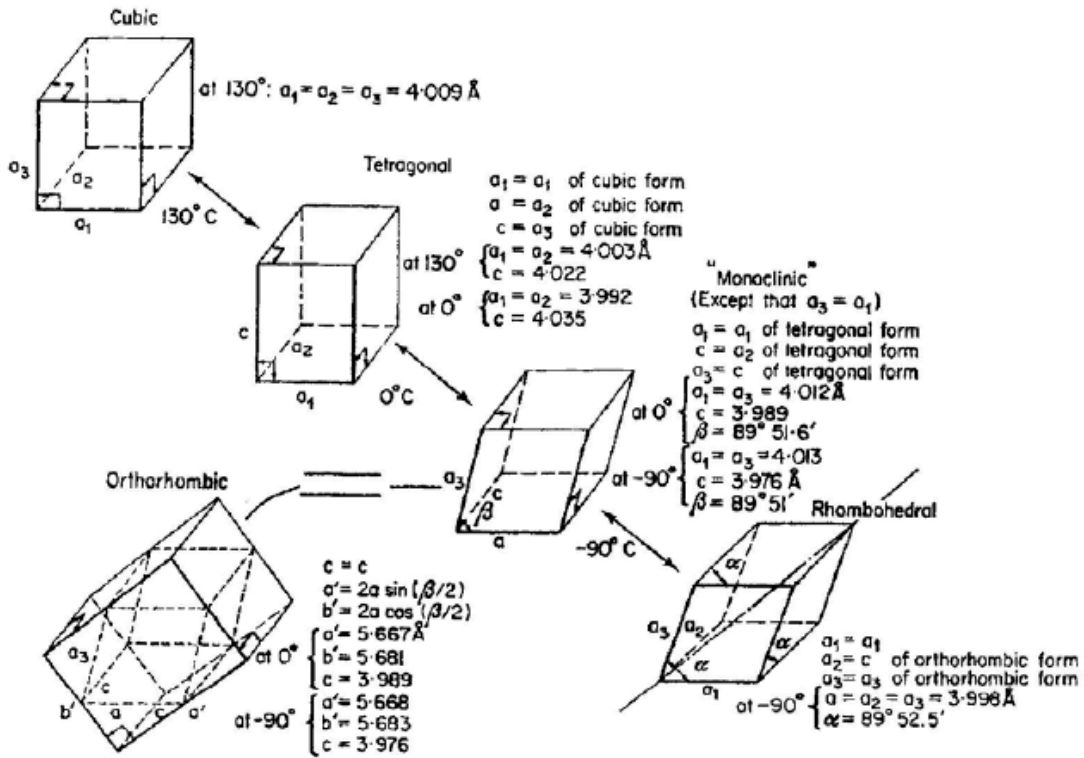

Figure 4.2 Distortion of $BaTiO_3$ unit cell showing temperature dependency [53].

In this chapter, the characterization outcomes of rf magnetron sputtering deposited BTO is being studied. Crystalline structure of BTO, nc-Ni, and NiO are examined by X-ray diffraction pattern analysis. Surface morphology, roughness, and electrical properties of these materials are shown in AFM results. Moreover, TEM micrographs demonstrate film nucleation as growth mechanisms, as well as its adhesion to the substrate.

4.1 Characterization

Figure 4.3 shows an XRD pattern of nc-Ni coated nickel disk, whereas Figure 4.4 is related to the same sample after BTO film deposition (sample# 1). The pattern demonstrates that after deposition of BTO, the grain size of nc-Ni interlayer increases slightly due to exposure to high temperature. Since the film thickness is lower than $100\,\mu$m, the x-ray diffractometry is performed on low angle mode while the sample angle is fixed on $\theta = 5°$.
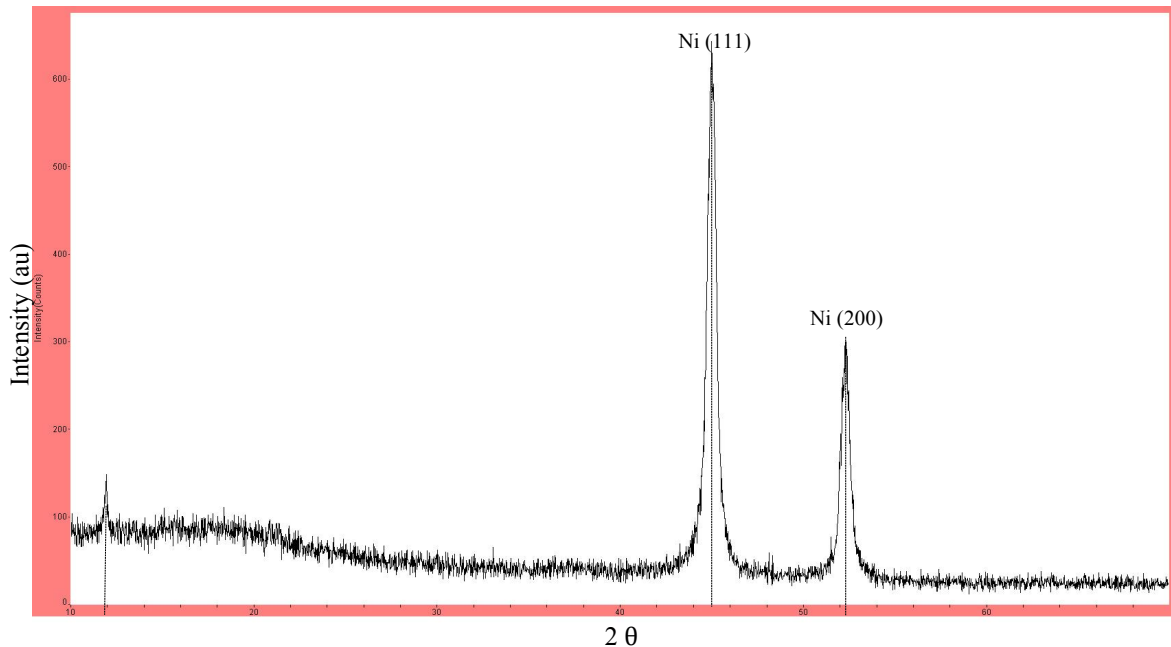

Figure 4.3 Low angle X-ray diffraction pattern of nc-Ni coated nickel disk.
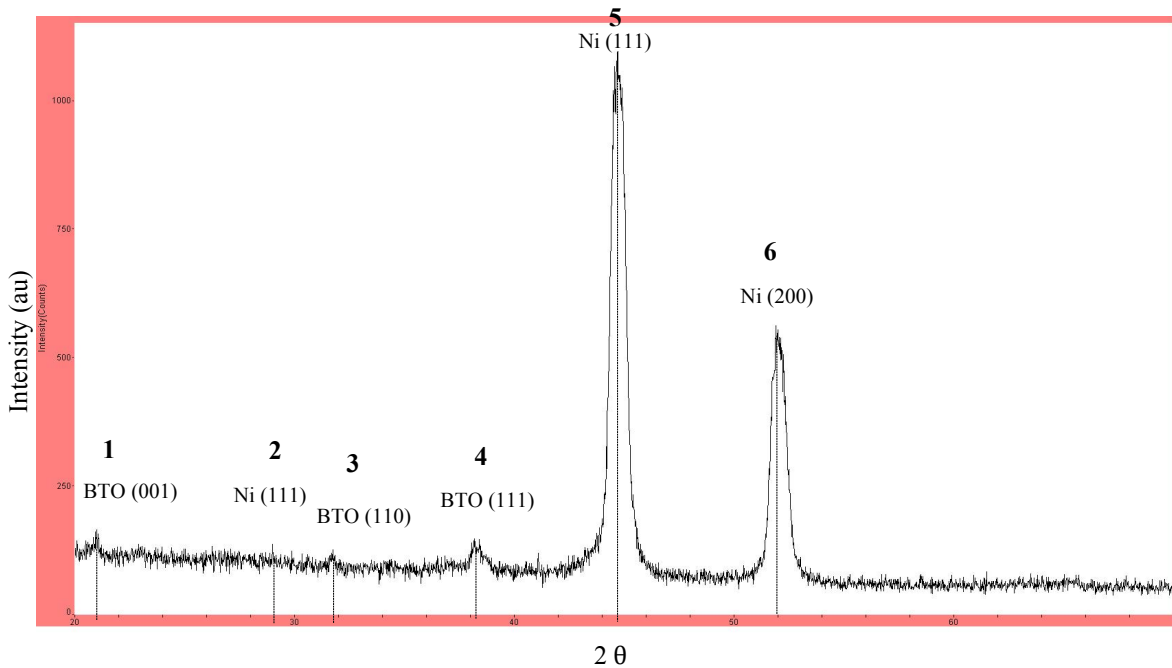
Figure 4.4 Low angle diffraction pattern of BTO coated nickel disk with nc-Ni interlayer (sample# 1).

As Figure 4.4 shows, peaks number 1, 3, and 4 are related to BTO. This figure shows that the deposited BTO film in sample#1 is amorphous and a deposition temperature of 350℃ is not high enough for producing crystalline BTO. The nc-Ni grain size, before and after deposition of BTO, as calculated by the Scherrer formula and is provided in Table 4.1.

Table 4.1 Grain size and structure of nc-nickel before and after BTO deposition in sample# 1

	nc-Ni Grain size	nc-Ni Structure	BTO Structure
Before BTO Deposition	17 nm	FCC	Amorphous
After BTO Deposition	21 nm	FCC	Amorphous

As shown in Table 4.1, the grain size of nc-Ni interlayer has increased during the BTO deposition, although it keeps its nanocrystalline characteristics. As it has been reported previously by Meletis et al. [54] annealing at temperatures > 350℃ causes grain growth in nc-Ni.

Figures 4.5 and 4.6 show XRD patterns of BTO coated nickel disk with NiO interlayer before and after BTO deposition, respectively (sample # 2). In order to synthesize a NiO layer, a nickel 200 disk was exposed to air at 750℃ in a tube furnace for 1hr. After BTO deposition, the grain size of NiO layer has increased slightly. Table 4.2 presents the calculated grain sizes of NiO before and after BTO deposition.
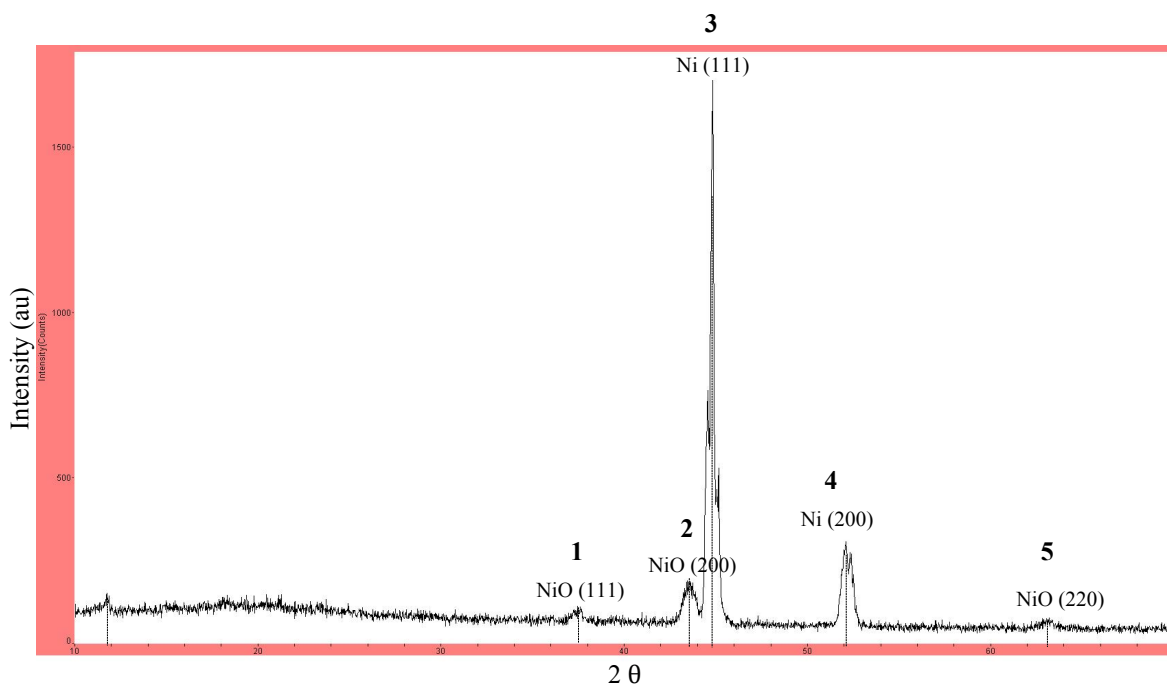
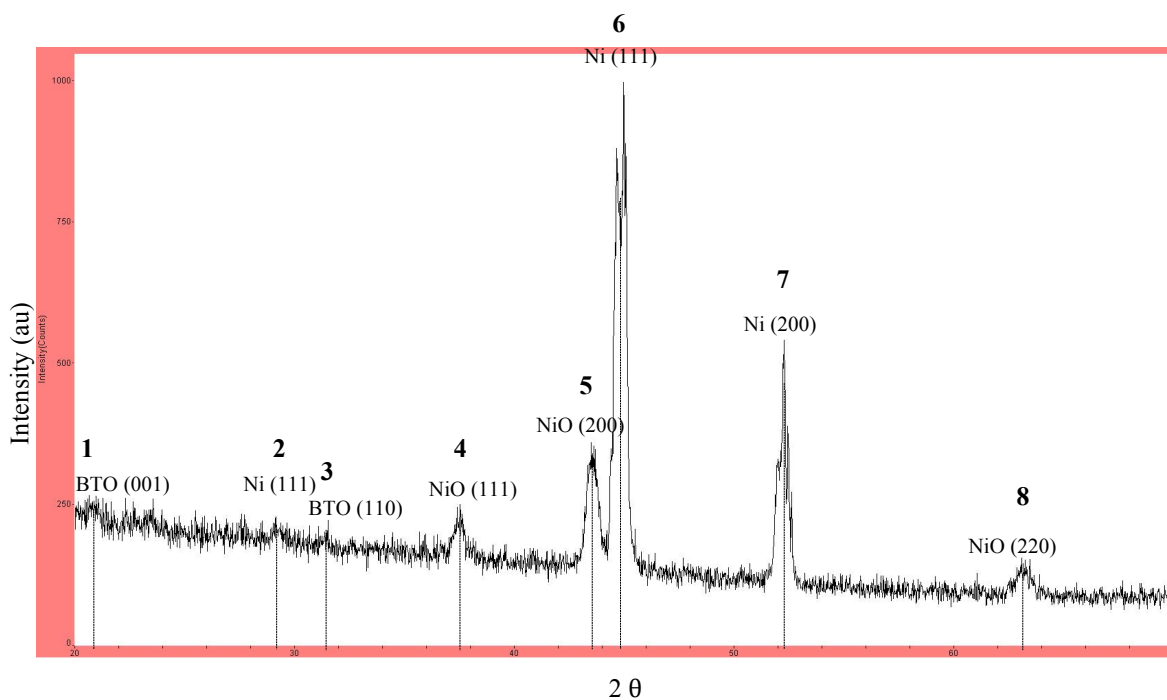Figure 4.5 Low angle X-ray diffraction pattern of NiO coated nickel disk.

Figure 4.6 Low angle X-ray diffraction pattern of BTO coated nickel disk with NiO interlayer (sample# 2).

Table 4.2 Grain size and structure of nickel oxid before and after BTO deposition in sample# 2

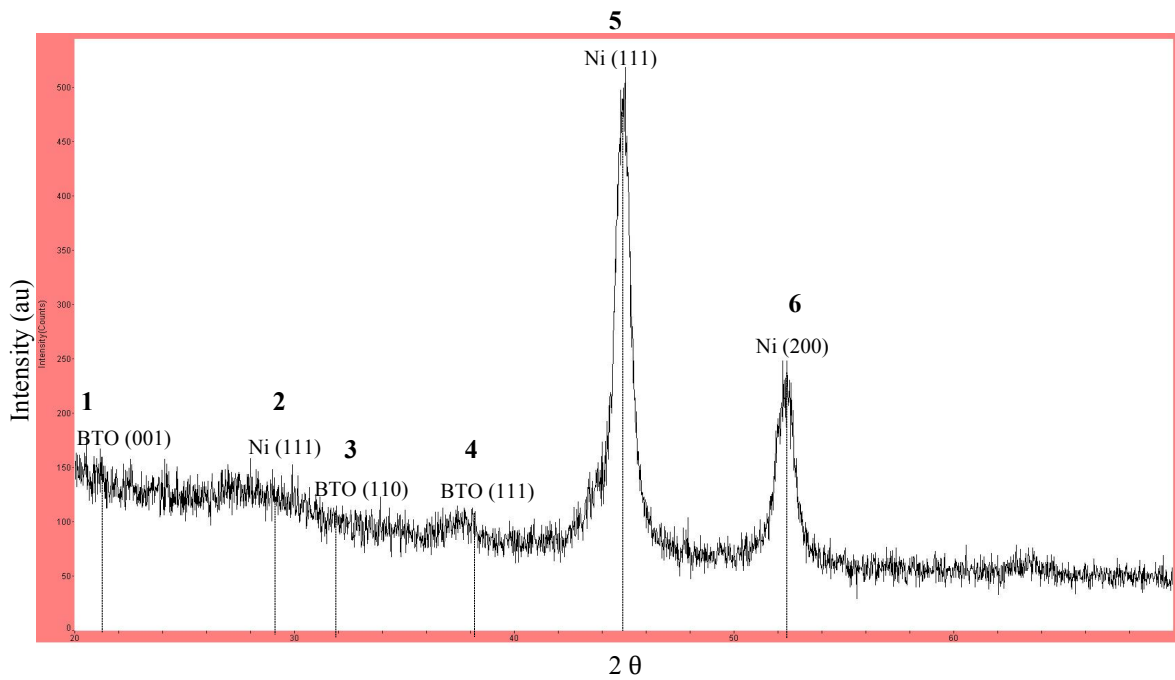|	NiO Grain size	NiO Structure	BTO Structure
Before BTO Deposition	15 nm	FCC	Amorphous
After BTO Deposition	18 nm	FCC	Amorphous

Figure 4.7 Low angle X-ray diffraction pattern of BTO coated silicon wafer with nc-Ni interlayer deposited at 350℃ (sample# 3).

Figure 4.7 presents the XRD pattern of sample# 3. As the XRD pattern shows and the TEM micrographs confirm, as-deposited BTO film on nc-Ni at 350℃ is majorly amorphous. Table 4.3 shows the slight grain size increase of nc-Ni during BTO deposition at 350℃.

Table 4.3 Grain size and structure of nc-nickel before and after BTO deposition in sample# 3

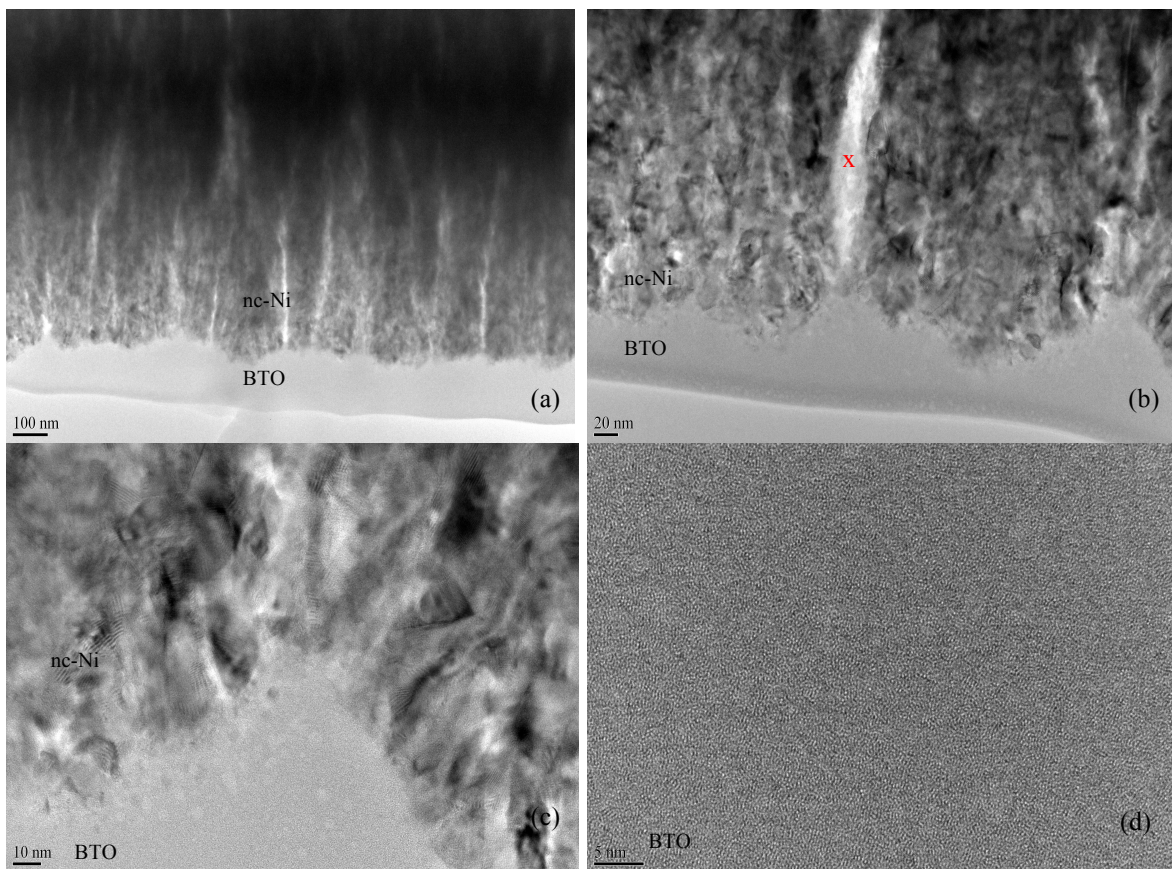|	nc-Ni Grain size	nc-Ni Structure	BTO Structure
Before BTO Deposition	17 nm	FCC	Amorphous
After BTO Deposition	21 nm	FCC	Amorphous

Figure 4.8 Cross-section TEM micrograph of sample# 3.

Figure 4.8 (a) gives an overall perspective of the amorphous BTO and columnar nc-Ni layers at low magnification. It can be observed in Figures 4.8 (b) and (c) that BTO has a conformal nature and penetrated into all the "valleys" of nc nickel surface forming mechanical kinks, which are anticipated to have a positive impact on the adhesion

between these two layers. Nc-Ni layer has a fine columnar structure and the BTO follows the surface topography without any evidence of interfacial void or discontinuities. Figure 4.8 (d) shows no diffraction constant which is consistent with the amorphous structure of BTO.

EDS results of the nickel and BTO layers presents the elements and their percentage in this sample.

Figure 4.8(d) shows the microstructure of BTO layer. After careful examination of this layer with different tilting angles under HRTEM and not observing any diffraction pattern, it is being clear that the BTO layer is amorphous.
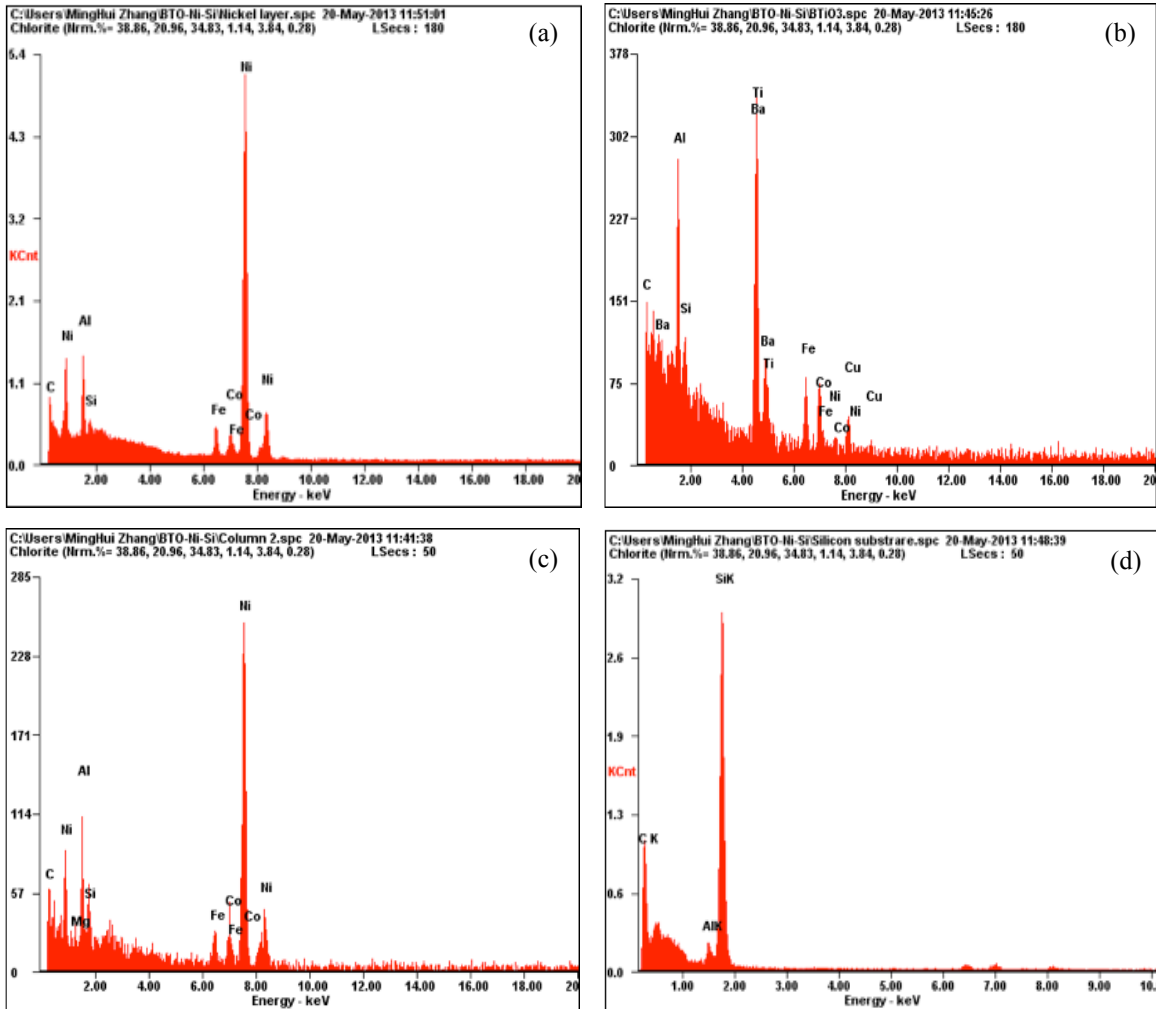

Figure 4.9 EDS results of (a) nickel layer, (b) BTO layer, (c) brighter column of Ni shown by x, and (d) silicon substrate.

Figure 4.10 presents the XRD pattern of sample# 4. Since nc-Ni deposition was followed by deposition of BTO, its grain size before exposing to high temperature was not measured. However, all the deposition conditions of nc-Ni on silicon wafer are similar to that of sample# 3. Therefore, it can be assumed that grain size of nc-Ni before BTO deposition of sample# 4 is similar to those of sample# 3, which is about 17 nm. Figure 4.10 shows that the crystallinity of BTO increases with raising the deposition temperature from 350℃ to 800℃. The deposited BTO on 350℃ (sample# 3) is amorphous, while the SADP pattern in figure 4.11(d) shows partial crystallinity in sample# 4. Moreover, higher deposition temperature provides potential energy for diffusion of oxygen from BTO to nanocrystalline nickel layer and formation of nickel oxide.

Table 4.4 Grain size and structure of nc-nickel and NiO before and after BTO deposition in sample# 4

	nc-Ni Grain size	NiO grain size	nc-Ni Structure	NiO Structure	BTO Structure
Before BTO Deposition	17 nm	N/A	FCC	FCC	Partially Crystalline
After BTO Deposition	25 nm	28 nm	FCC	FCC	Partially Crystalline
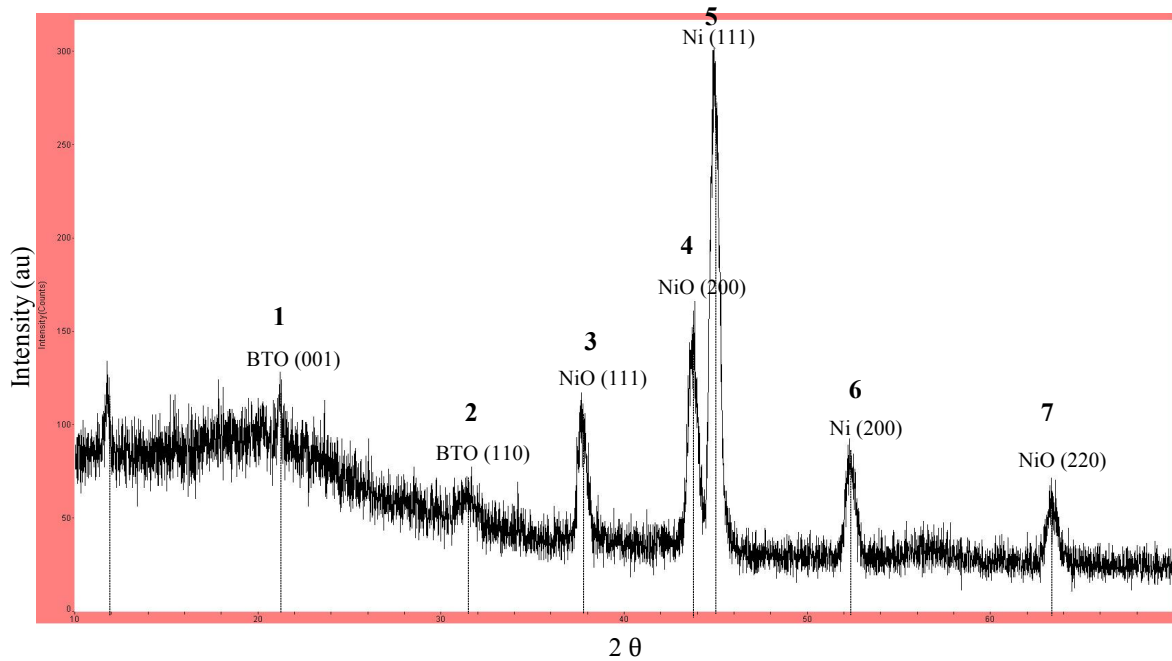
Figure 4.10 Low angle X-ray diffraction pattern of BTO coated silicon wafer with nc-Ni interlayer deposited at 800°C (Sample# 4).

The micrograph observation and SADP shown in Figure 4.11 suggest that BTO has started crystalline nucleation at some places but the nuclei did not have enough time to grow completely. Moreover, the nickel oxide layer formed on the surface of nc-Ni layer has FCC crystalline structure, which could be helpful in the matter of the adhesion of BTO film to the nc-Ni layer.

Figure 4.11 Cross-section TEM micrograph of sample# 4.
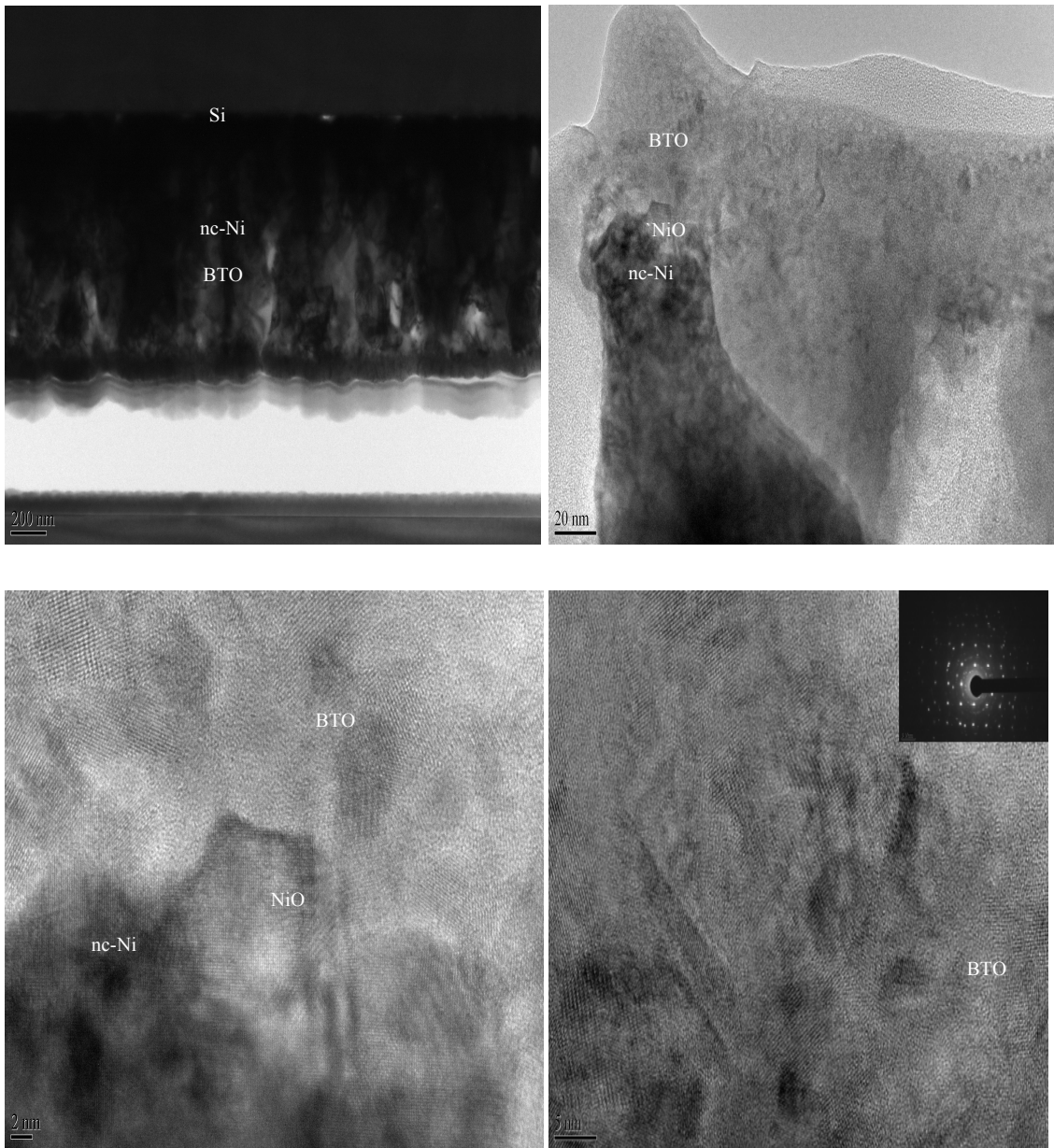
Figures 4.12 to 4.15 show AFM of the surface morphology of as deposited BTO on different substrates with different buffer layers.
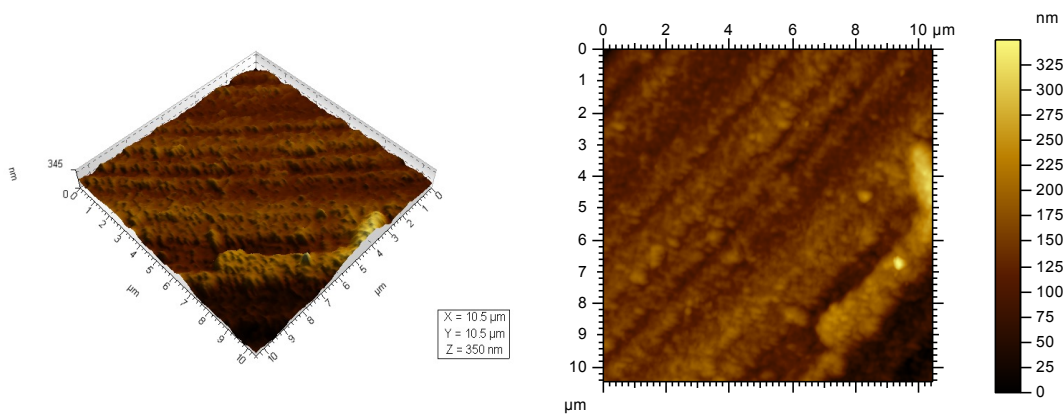

Figure 4.12 Surface morphology of BTO coated nickel disk with nc-Ni interlayer (sample# 1).
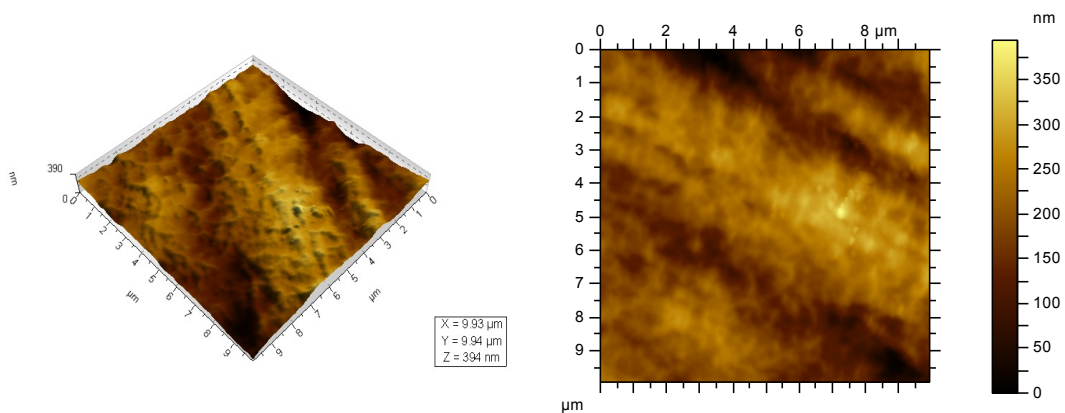
Figure 4.13 Surface morphology of BTO coated nickel disk with NiO interlayer (sample# 2).

As it is shown in these Figures, the NiO interlayer includes roughness to the final surface, while the BTO layer deposited on the nc-Ni buffer layer has lower surface roughness. However, comparing Figure 4.12 to 4.14 shows that the surface roughness of the samples deposited on Si wafer substrate is lower than the ones deposited on nickel disks.

The rougher surface demonstrated in Figure 4.15 comparing to Figure 4.14 might be due to the formation of thin layer of NiO at the interface of nc-Ni and BTO layers.

Figure 4.14 Surface morphology of BTO coated silicon wafer with nc-Ni interlayer deposited at 350°C (sample# 3).

Figure 4.15 Surface morphology of BTO coated silicon wafer with nc-Ni interlayer deposited at 800°C (Sample# 4).

Chapter 5

CONCLUSION

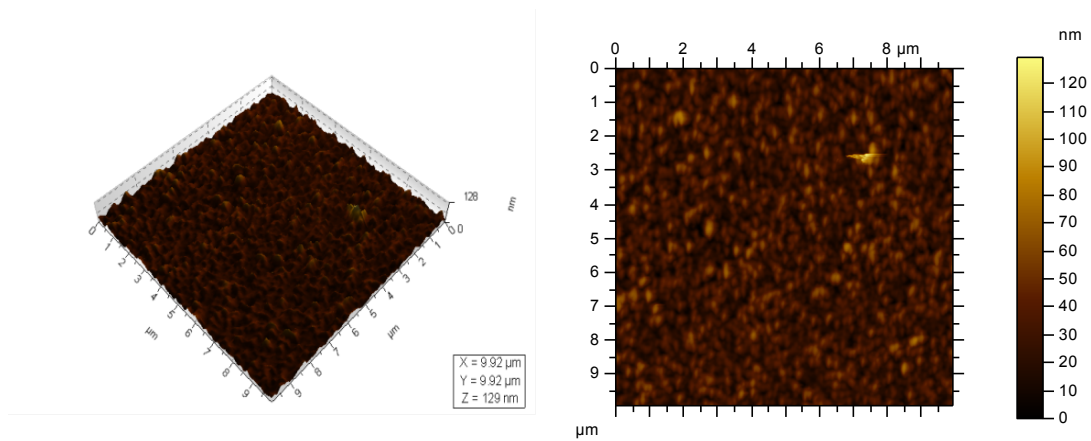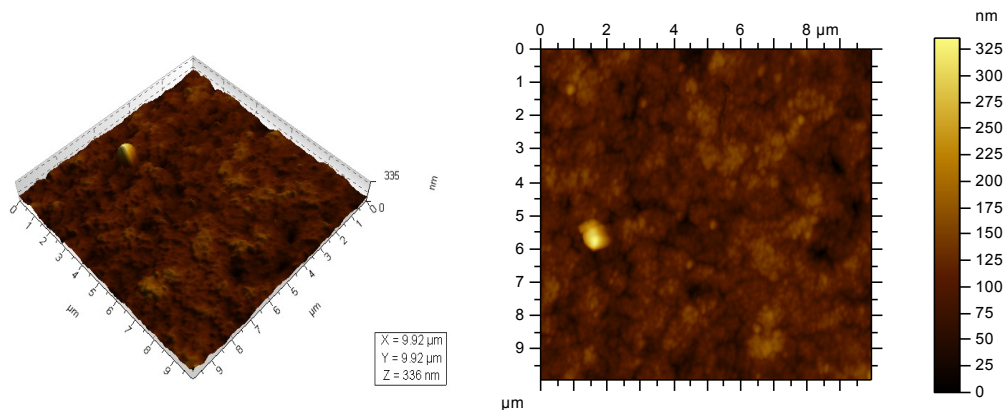Barium titanate has been deposited on nickel disks and silicon wafer substrates by magnetron sputtering at two different temperatures; 350℃ and 800℃. In order to facilitate this deposition, two different buffer layers were used: nanocrystalline nickel and nickel oxide. These interfacial layers are nanocrystalline and can benefit the deposition of BTO on the bulk polycrystalline substrates. Although deposition of BTO increases the buffer layers grain size, they still remain nanocrystalline and keep nanoproperties. Since in nc-Ni layer the grain boundary density is higher than bulk materials, high energy locations for BTO grain nucleation and growth are of higher density. Moreover, due to small size of grains, kinks and mechanical attachments can assist the adhesion of BTO layer to nc Ni. As it can be shown from TEM diffraction patterns, the crystallinity of as deposited BTO layer increases by increasing the sputtering temperature. Furthermore, at higher temperature of BTO deposition, oxygen can diffuse from BTO layer into nc-Ni. This causes oxidation of a thin layer of nc-Ni and formation of NiO layer at the interface of BTO and nc-Ni films.

The AFM results demonstrate that the samples deposited on silicon wafer substrates have lower surface roughness compared to the ones deposited on nickel disks. Also, nc-Ni buffer layer improves the surface roughness, while NiO interlayer makes the final surface rougher. Furthermore, the thin NiO layer formed by diffusion of oxygen between nc-Ni and BTO films might change the as deposited BTO morphology and roughness.

It can be concluded from the microcrystalline studies and diffraction analysis that nc nickel can be used as an interfacial buffer layer, facilitating BTO growth on nickel substrate.

REFERENCES

1. T. Sumi, Y. Judai, K. Hirano, T. Ito, T. Mikawa, M. Takeo, M. Azuma, S. Hayashi, Y. Uemoto, K. Arita, T. Nasu, Y. Nagano, A. Inovr, A. Matsuda, E. Fuji, Y. Shimnda, and T. Otsuki, Jpn. J. Appl, Phys. 35 (1996) 1516.

2. Yu.A. Boikov, Z.G. Ivanov, A.N. Kiselev. E. Olsson, and T. Gleason, J. Appl. Phys. 78 (1995) 4591.

3. G. Arlt, D. Henning, and G. de With, J. Appl. Phys. 58 (1985) 1619.

4. H.A. Lu, L.A. Wills, and B.W. Wessels, Appl. Phys. Lett. 64 (994) 2973.

5. A.S. Bhalla and K.M. Nair (Eds.), Ceramic Transactions, Vol. 25. Ferroelectric Thin Films, American Ceramic Society, 1992.

6. R. Thomas, D.C. Dube, M.N. Kamalasananb, and S. Chandra, Thin Solid Films 346 (1999) 212-225.

7. A. Ianculescua, M. Gartnerb, B. Despaxc, V. Bleyc, Th. Lebeyc, R. Gavrila, and M. Modreanu, Appl. Surface Sci. 253 (2006) 344-348.

8. L. Preda, L. Courselle, B. Despax, J. Bandet, and A. Ianculescu, Thin Solid Films 389 (2001) 43-50.

9. J. Berge, A. Vorobieva, and S. Gevorgian, Thin Solid Films 515 (2007) 6302-6308.

10. Y. Yang, J. Shi, W. Huang, S. Dai, and L. Wang, Mater. Lttr. 56 (2002) 1048-1052.

11. Q.X. Jia, L.H. Changb, and W.A. Andersonb, Thin Solid Films 259 (1995) 264-269.

12. K.S. Sree Harsha, "Principles of Physical Vapor Deposition of Thin Films", Elsevier, 2006.

13. M. Ohring, " The materials Science of Thin Films", Academic Press, 1991.

14. L.I. Maissel and R. Glang, "Handbook of Thin Film Technology, McGraw-Hill, 1970.

15. S. Brunauer, "The adsorption of Gases and Vapors", Vol. 1, Physical Adsorption, Princeton University Press, 1945.

16. L.E. Murr, "Interace Phenomena in Metals and Alloys", Addison-Wesley, 1975.

17. E.D. Hondros, "Precipitation Process in Solids", The Metallurgical Society of AIME, 1978.

18. M. Ohring, "Material Science of Thin Films: Deposition and Structure", Academic Press. xxi, 2002.

19. D.L. Smith, "Thin Film Deposition: Principles and Practice", McGraw-Hill. Xxxiii, 1995.

20. W.D. Westwood, "Sputter Deposition", AVS Monographs, 2003.

21. S.M. Aygun, "Processing Science of Barium Titanate", PhD Thesis at North Carolina State University, 2009.

22. Yuhuan, "Ferroelectric Materials and Their Applications", Elsevier, 1991.

23. W.J. Leng, C.R. Yang, J.H. Zhang, H.W. Chen, H. Ji, "Structural and optical properties of $Ba_xSr_{1-x}TiO_3$ thin films on indium tin oxide/quartz substrates prepared by radio-frequency magnetron sputtering", J. of Appl. Phys., 2006.

24. E.J. Cukauskas, S.W. Kirchoefer, W.J. DeSisto, J.M. Pond, "$Ba_{1-x}Sr_xTiO_3$ thin films by off-axis cosputtering $BaTiO_3$ and $SrTiO_3$", J. of Appl. Phys., 1999.

25. F.M. Pontes, E.R. Leite, D.S.L Pontes, and E. Longo, J. of Appl. Phys. 91, 5972

(2002).

26. J.M. Pond, S.W. Kirchoefer, W. Change, J.S. Horwitz, and D.B. Chrisey, Integr. Ferroelectr. 22, 317 (1998).

27. D.L. Polla and L.F. Francis, Annu. Rev. Mater. Sci. 28 (1998) 563.

28. B. Fan, G. Song, and F. Hussain, Smart Mater. Struct. 14 (2005) 400.

29. Z. Yuan, J. Liu, J. Weaver, C.L. Chen, J.C. Jiang, B. Lin, V. Giurgiutiu, A. Bhalla, and R.Y. Guo, Appl. Phys. Lett. 90 (2007) 202901.

30. A. Garcia and V. Vanderbilt, Appl. Phys. Lett. 72 (1998) 2981.

31. M. H. Frey and D. A. Payne, Phys. Rev. B 54 (1996) 3158.

32. J.C. Jiang, E.I. Meletis, Z. Yuan, J. Liu, J. Weaver, C.L. Chen, B. Lin, V. Giurgiutiu, R.Y. Guo, A.S. Bhalla, D. Liu, and K.W. White, J. Nano Research 1 (2008) 59-63.

33. Z. Grubac, Z. Petrovic, J. Katic, M. Metikos-Hukovic, and R. Babic, Journal of Electroanalytic Chem. 645 (2010) 87-93.

34. R. Rofagha, R. Langer, A.M. El-Sherik, U. Erb, G. Palumbo, and K.T. Aust, Scripta Metall. Mater, 25 (1) (1999) 2867-2872.

35. R. Mishra and R. Balasubramanian, Corros. Sci. 46 (2004) 3019-3029.

36. M.R. Zamanzad-Ghavidel, K. Raeissi, and A. Saatchi, Mater. Lett. 63 (2009) 1807-1809.

37. H. Zhao, L. Liu, J. Zhu, Y. Tang, and W. Hu, Mater. Lett. 61 (2007) 1605-1608.

38. L. Wang, J. Zhang, Y. Gao, Q. Xue, L. Hu, and T. Xu, Scripta Mater. 55 (2006) 657-660.

39. M. Metikos-Hukovic, Z. Grubac, N. Radic, and A. Tonejc, Journal of Molecular Catalysis A: Chemical 249 (2006) 172-180

40. L. Liu, Y. Li, and F. Wang, Electrochimica Acta 53 (2008) 2453-2462.

41. S. Geng, F. Wang, and S. Zhang, Surface and Coating Technology 167 (2003) 212-216.

42. R.C. Hugo, H. Kung, J.R. Weertman, R. Mitra, J.A. Knapp, and D.M. Follstaedt, Acta Materialia 51 (2003) 1937-1943.

43. C.C. Koch, D.G. Morris, K. Lu, A. Lnoue, Mater. Res. Soc. Bull. 24 (1999) 54-58.

44. R.Z. Valiev, I.V. Alexandrov, Y.T. Zhu, T.C. Lowe, J. Mater. Res. 17 (2002) 5-8.

45. X.X. Shen, C.D. Gu, J.S. Lian, Q. Jiang, Z.H. Jiang, L.Y. Qin, J. Appl. Phys. 108 (2010) 054319.

46. S. Cheng, E. Ma, Y.M. Wang, L.J. Kecskes, K.M. Youssef, C.C. Koch, U.P. Trociewitz, K. Han, Acta Mater. 53 (2005) 1521-1533.

47. X.X. Shen, J.S. Lian, Z.H. Jiang, Q. Jiang, Mater. Sci. Eng. A 487 (2008) 410-417.

48. D. Wolf, V. Yamakov, S.R. Phillpot, A.K. Mukherjee, H. Gleiter, Acta Mater. 53 (2005) 1-40.

49. U. Erb, Electrodeposited Nanosrystals, Nanostruct. Mater. 6 (1995) 533-538.

50. X. Shen, Z. Xu, J. Lian, Q. Jiang, Mater. Sci. Eng. A 528 (2011) 7878-7886.

51. Jie He, PhD Thesis, University of Texas at Arlington, (2012) 55.

52. B.C. Frazer, H.R. Danner, and P. Pepinsky, Phys. Rev. 100 (1955) 745.

53. H.F. Kay and P. Vousden, Phil. Mag. 40 (1949) 1019.

54. D. Guidry, J.C. Jiang, K. Lian, and E.I. Meletis, J. Nanosci. Nanotech. 9 (2009) 4227-4232.

BIOGRAPHICAL INFORMATION

Parisa Sahebi was born on September 21, 1989 in Mashhad, Iran. She received her bachelor degree in Materials Science and Engineering from Sharif University of Technology in 2011. After that, she got admitted to The University of Texas at Arlington for graduate studies and she received her master degree in Materials Science and Engineering in 2013. During her undergrad studies in Sharif University of Technology, she worked at Solidification and Casting Laboratory under the supervision of Dr. Ashouri. She focused on semi-solid joining of Aluminum alloys and studied the effect of heat treatment and additives on physical and mechanical properties of the joint parts. During her graduate study in University of Texas at Arlington, she joined Surface and Nano Engineering group and worked under supervision of Dr. Meletis. Her researched focused on effect of nanocrystalline interlayer on integration of ferroelectric Barium Titanate thin films on Nickel and Silicon wafer substrates. Her ability in materials characterization and analysis provides her the opportunity to achieve a high quality research level and address challenges in materials science.